JCI insight

RESEARCH ARTICLE

Rb1/Rbl1/Vhl loss induces mouse subretinal angiomatous proliferation and hemangioblastoma

Ran Wei,[1,2] Xiang Ren,[1,2] Hongyu Kong,[1,2] Zhongping Lv,[1,2] Yongjiang Chen,[3,4] Yunjing Tang,[1,2] Yujiao Wang,[1,2] Lirong Xiao,[1] Tao Yu,[4] Sabiha Hacibekiroglu,[4] Chen Liang,[1] Andras Nagy,[4] Rod Bremner,[3,4] and Danian Chen[1,2,3,4]

[1]Research Laboratory of Ophthalmology and Vision Sciences, State Key Laboratory of Biotherapy, and [2]Department of Ophthalmology, West China Hospital, Sichuan University, Chengdu, China. [3]Lunenfeld-Tanenbaum Research Institute, Sinai Health System, and Departments of Ophthalmology and Visual Science, and Laboratory Medicine and Pathobiology, University of Toronto, Toronto, Ontario, Canada. [4]Lunenfeld-Tanenbaum Research Institute, Sinai Health System, and Institute of Medical Science, University of Toronto, Toronto, Ontario, Canada.

Von Hippel–Lindau (Vhl) protein inhibits hypoxia-inducible factor (Hif), yet its deletion in murine retina does not cause the extensive angiogenesis expected with Hif induction. The mechanism is unclear. Here we show that retinoblastoma tumor suppressor (Rb1) constrains expression of Hif target genes in the *Vhl*$^{-/-}$ retina. Deleting *Rb1* induced extensive retinal neovascularization and autophagic ablation of photoreceptors in the *Vhl*$^{-/-}$ retina. RNA-sequencing, ChIP, and reporter assays showed Rb1 recruitment to and repression of certain Hif target genes. Activating Rb1 by deleting cyclin D1 induced a partial defect in the retinal superficial vascular plexus. Unexpectedly, removing *Vhl* suppressed retinoblastoma formation in murine *Rb1/Rbl1*–deficient retina but generated subretinal vascular growths resembling retinal angiomatous proliferation (RAP) and retinal capillary hemangioblastoma (RCH). Most stromal cells in the RAP/RCH–like lesions were Sox9^{+}, suggesting a Müller glia origin, and expressed Lgals3, a marker of human brain hemangioblastoma. Thus, the Rb family limit Hif target gene expression in the *Vhl*$^{-/-}$ retina, and removing this inhibitory signal generates new models for RAP and RCH.

Introduction

Retinal neovascularization is associated with multiple disorders such as retinopathy of prematurity, diabetic retinopathy, and age-related macular degeneration (AMD) (1, 2). Retinal angiomatous proliferation (RAP) is one form of neovascular AMD, which is a leading cause of blindness in the world (3). Neovascular AMD also includes 2 other forms, typical choroidal neovascularization (CNV) and polypoidal choroidal vasculopathy. RAP arises from deep retinal capillaries and develops from intraretinal (stage I), to subretinal (stage II), and finally to choroidal neovascularization and retinal–choroidal anastomosis (stage III) (4). Pathologically, RAP is an intraretinal angiomatous complex within the outer retina (5, 6). Although RAP follows a different natural course and response to treatment from typical CNV, few animal models are established to allow us to fully understand the pathogenesis or to test new treatments for late-stage disease, even though there are several mouse models of early-stage RAP (7–11).

Retinal capillary hemangioblastoma (RCH) is the hallmark lesion of ocular von Hippel–Lindau (VHL) disease (12). This multisystem tumor syndrome is caused by germline *Vhl* gene mutations and is also associated with many other tumors, such as brain hemangioblastoma and clear cell renal cell carcinomas (CCRCCs) (13). Vhl protein is a component of the E3 ubiquitin ligase complex that targets hypoxia-inducible factor–α (Hif-α) for proteasomal degradation. Hif is the master regulator of the response to hypoxia because Hif-α accumulates and induces the transcription of genes involved in adaptation to hypoxia, including BCL2 interacting protein 3 (*Bnip3*), erythropoietin (*Epo*), and *Vegfa* (14). Angiogenesis is critical for adaptation to hypoxia and retinal development and also influences or drives many retinal diseases. In murine newborn eyes, the hyaloid vessels in the vitreous regress, and the retinal vessels develop to supply blood to the retina (15). The retinal vasculature consists of 3 parallel

Authorship note: RW, XR, HK, ZL, and YC contributed equally to this work.

Conflict of interest: The authors have declared that no conflict of interest exists.

Submitted: January 31, 2019
Accepted: October 10, 2019
Published: November 14, 2019.

Reference information: *JCI Insight*. 2019;4(22):e127889. https://doi.org/10.1172/jci.insight.127889.

vascular plexuses, including the superficial vascular plexus (SVP) in the nerve fiber layer, deep vascular plexus (DVP) in the outer plexiform layer (OPL), and intermediate vascular plexus (IVP) in the inner plexiform layer (16).

The origin of the true tumorigenic cell type in RCH and RAP is controversial. This reflects the dearth of human samples available for histopathological analyses, limiting the vast majority of studies to observations in intact human eyes. In RCH, early work referred to an astrocytic component (17). More recently, but with only 3 cases, 2 groups reported that glial fibrillary acidic protein–positive ($GFAP^+$) glial cells contribute to human RCH (18, 19). Thus, the cell of origin of human RCH needs further investigation.

Deleting *Vhl* in murine retina delays regression of hyaloid vessels and inhibits retinal angiogenesis, which depend on the associated high levels of Hif-1α (20, 21). Paradoxically, therefore, high Hif does not induce RCH, but instead inhibits retinal angiogenesis in the murine $Vhl^{-/-}$ retina. Deleting *Vhl* in all retinal cells and vascular endothelial cells using $UBC\text{-}Cre^{ER}$ also suppresses retinal angiogenesis (22). Deleting *Vhl* in specific retinal cell types, such as amacrine or horizontal interneurons (23), rods (24), cones (25), or retinal pigment epithelium (RPE) cells (26), also does not induce RCH. Although removing *Vhl* in murine hemangioblasts using stem cell leukemia–Cre^{ER} ($Scl\text{-}Cre^{ER}$) triggered some features of early-stage RCH, including dilated tortuous vessels, vascular leakage, and foamy stromal cell clusters, histologically it did not cause any neovascularization or hemangioblastoma structures in the retina (27). Thus, it remains unclear why the $Vhl^{-/-}$ retina lacks vascular overgrowth and RCH. One possibility is that inhibitors interfere with Hif activity. Indeed, an SNP microarray study implicated several cell cycle genes in the pathogenesis of hemangioblastoma, including the retinoblastoma repressor (Rb1) (28). Inactivating *Vhl* plus additional tumor suppressors (*Rb1* and tumor protein p53; *Tp53*) can induce CCRCC (29). However, inhibitors that block angiogenesis in the $Vhl^{-/-}$ murine retina are unknown.

In addition to angiogenesis, autophagy is important for hypoxia adaptation because it captures and degrades intracellular components to sustain metabolism and homeostasis (30). Hypoxia-induced autophagy requires the constitutive expression of beclin 1 (Becn1) and autophagy related 5 (Atg5) and the Hif1-dependent expression of Bnip3/Bnip3L (30, 31). Autophagy has been observed in human RCH (32), but its role in the $Vhl^{-/-}$ murine retina is unclear.

Retinoblastoma is the most common pediatric intraocular tumor. Rb1 regulates cell cycle, cell death, and many other cellular processes in part by inhibiting the E2f transcription factors (33). Loss of *Rb1* and its relative *Rbl1* (also called *p107*) in the retina causes mouse retinoblastoma (34–36). In the *Rb1/Rbl1*–null retina, all differentiating cells divide ectopically, excitatory neurons (ganglion cells, bipolar cells, rods, and cones) undergo apoptosis, while inhibitory neurons (horizontal and amacrine cells) and Müller glia survive, and retinoblastoma arises from the amacrine cell lineage (34). Rb1 can bind to the promoter and repress the expression of *Bnip3*, an Hif-1 target gene (37), and there are E2f binding sites in the promoter of several proangiogenic Hif targets (38), raising the possibility that Rb1 might be the unknown inhibitor that counters Hif activity in the $Vhl^{-/-}$ retina. However, there is also in vitro work suggesting that Rb1 binds and potentiates Hif-1 (39), although this has not been reproduced by others. We showed that Rb1 is required for the formation of intraretinal vascular plexuses (40). Nevertheless, this defect is indirect because it is rescued by deleting BCL2-associated X protein (*Bax*) and blocking neuronal cell death (40). Thus, whether Rb1 has a separate direct role in constraining Hif activity and angiogenesis is unclear.

The *Ccnd1* gene encodes cyclin D1, a regulatory subunit of the holoenzyme that phosphorylates and inactivates Rb1. The retina has high levels of cyclin D1 that keep Rb1 inactive in retinal progenitors (41). $Ccnd1^{-/-}$ mice exhibit a hypocellular retina because of premature cell cycle exit of retinal progenitor cells (41). Whether cyclin D1 influences retinal angiogenesis is unknown.

We utilized genetics, RNA-sequencing, ChIP, and reporter assays to address these questions. Strikingly, *Rb1* deletion in the $Vhl^{-/-}$ retina triggered both extensive retinal neovascularization and photoreceptor autophagy. These Rb1 functions were linked to direct binding and repression of Hif target genes in the retina. Moreover, activating Rb1 in $Ccnd1^{-/-}$ retina induced an SVP defect. Unexpectedly, *Vhl* loss suppressed murine retinoblastoma by inhibiting ectopic division in the cell of origin, allowing us to assess the effect of removing both *Rb1/Rbl1* and *Vhl* on angiogenesis without the confounding effects of tumorigenesis. Notably, the *Rb1/Rbl1/Vhl*–triple null retina exhibited subretinal lesions that resemble human late-stage RAP (5, 6) and RCH (12). Most stromal cells in the RAP/RCH–like lesions were $Sox9^+$ and galectin $Lgals3^+$, suggesting a Müller glia origin. Our study reveals potentially new roles for Rb1 in constraining *Vhl*-null–induced retinal angiogenesis and autophagy, establishes a mouse model of RCH and late-stage RAP, and links the Rb pathway to vessel growth associated with neovascular AMD and VHL disease.

Results

Rb1 suppresses angiogenesis in the Vhl-null retina. To delete floxed (^{fl}) *Rb1* or *Vhl* alleles (20, 21, 34), we used the *α-Cre* transgene, which is active from E10 in peripheral retinal progenitors (42). We bred *α-Cre Rb1$^{fl/fl}$* (*Rb1*-KO) mice with *Vhl$^{fl/fl}$* mice and quantified vessel growth using the endothelial marker isolectin B4 (IB4). As reported before (20, 21), *α-Cre Vhl$^{fl/fl}$* (*Vhl*-KO) mice demonstrated increased level of Hif-1α protein (Supplemental Figure 1; supplemental material available online with this article; https://doi.org/10.1172/jci.insight.127889DS1) and delayed regression of hyaloid vessels and retinal angiogenesis, but unlike VHL patients, lacked any evidence of vascular overgrowth, except a few vessels invaded into the outer nuclear layer (ONL) (Figure 1, A and B). Indeed, the protein levels of Vegfa and kinase insert domain receptor (Kdr) were normal (Supplemental Figure 1). In the *Rb1/Vhl*–double knockout (DKO) retina, hyaloid vessel regression was still delayed, but strikingly, there were many new blood vessels in the peripheral retina (Figure 1, A and B). These vessels penetrated throughout all retinal layers to form a dense capillary bed, and there was no normal SVP, IVP, or DVP (Figure 1B). To compare the vascular density to other genotypes, we used vascular images taken from similar depths below the ganglion cell layer (GCL) to represent the IVP and DVP for the DKO retina. The vascular density was 3–4 times higher than in WT retina (Figure 1, B and C).

These new blood vessels began to form at around P8, likely originating from both the existing retinal vasculature and the persistent hyaloid vessels (Supplemental Video 1), because they were linked to hyaloid vessels (Figure 1D, arrowheads) and the DVP in the central retina (Figure 1D, arrows). In the middle of the new vessel bed, there were many IB4$^+$ "grape-like" clusters of endothelial cells (Figure 1, E and F). As the delayed hyaloid vessels blocked the fluorescein signal (Figure 1G), the retinal blood vessels of the live animal in fundus fluorescein angiography (FFA) were not clear, but neovascularization and vascular leakage could be documented at late stages (Figure 1H, arrows). Retroorbital injection of FITC-dextran (43) demonstrated that the new vessels were leaking and clearly shunted to the persistent hyaloid vessels (Figure 1I). These new vessels persisted for at least 2 years (Figure 1J).

Rb1 loss alone causes apoptosis of certain retinal neurons, which indirectly impedes angiogenesis (40). Cell loss is unlikely to explain the excessive angiogenesis in the *Rb1/Vhl*–null retina. However, in addition, *Rb1* loss causes a transient period of ectopic division of all retinal cell types and disrupts lamination (34, 40). To examine whether any of these *Rb1*-null phenotypes might explain the excessive vasculature in the *Rb1/Vhl*–null retina, we took 2 genetic approaches. The *Rb1$^{+/-}$* retina is WT (34); thus we assessed the effect of removing 1 *Rb1* allele on angiogenesis. Notably, this subtle genetic manipulation still induced retinal neovascularization in the *Vhl$^{-/-}$* retina (Figure 1, A–C). Moreover, vessel density was lower than in the *Rb1/Vhl*–DKO retina, revealing a dose-dependent role for Rb1 in limiting angiogenesis. Second, we assessed the effect of E2f1 on angiogenesis. Rb1 binds and inhibits E2f, and deleting *E2f1* rescues all the ectopic cell division, cell death, and lamination defects seen in the *Rb1*-null retina (40, 44). Importantly, *E2f1* deletion did not rescue neovascularization in the *Rb1/Vhl*–DKO retina (Figure 1, A–C). Together, these *Rb1$^{+/-}$* and *E2f1$^{-/-}$* data suggest that Rb1 inhibits vessel growth in the *Vhl$^{-/-}$* retina independent of its roles in controlling cell division, apoptosis, or lamination.

Rb1 suppresses loss of Vhl-null photoreceptors. The above data show that deleting *Rb1* unleashes the pro-angiogenic effects associated with *Vhl* loss. Potentially, therefore, Rb1 also suppresses other phenotypes in this context. For example, although the number of all retinal cell types was normal in P18 *Vhl*-KO retina (Figure 2, A–D), there is modest loss of photoreceptors in the *Vhl$^{-/-}$* retina around P30 (20). But whether Rb1 limits this phenotype is unknown.

To assess this issue, we stained the P18 *Rb1/Vhl*–DKO retina with cell type–specific markers. As in the *Rb1$^{-/-}$* tissue, the DKO retina was missing ganglion (Pou4f2$^+$) and rod bipolar (Pkca$^+$) cells (Figure 2, A and B, and Supplemental Figure 2). Whereas the *Rb1$^{-/-}$* retina retained many rod (Rho$^+$) and all cones (Arr3$^+$) as reported before (34), all photoreceptors were absent in the DKO tissue (Figure 2, A and B, and Supplemental Figure 2). To exclude the possibility that these neurons never formed in the DKO retina, we stained P0 DKO retina with Pou4f2, Crx (precursors of rod, cone, and bipolar cells), and Thrb2 (precursor of cones) (Supplemental Figure 3). Obviously all these neurons formed in the DKO retina. Thus, all *Rb1/Vhl*–null excitatory neurons are generated but then die, indicating that *Rb1* and *Vhl* loss are synthetically lethal to photoreceptors.

Similar to the *Rb1$^{-/-}$* tissue, the P18 *Rb1/Vhl*–DKO retina retained inhibitory amacrine (Ap2a$^+$) and horizontal (Onecut2$^+$) neurons, as well as Müller glia (Sox9$^+$), and while the DKO tissue had similar numbers of horizontal cells, there were modest increases in the proportion of amacrine cells (~2-fold)

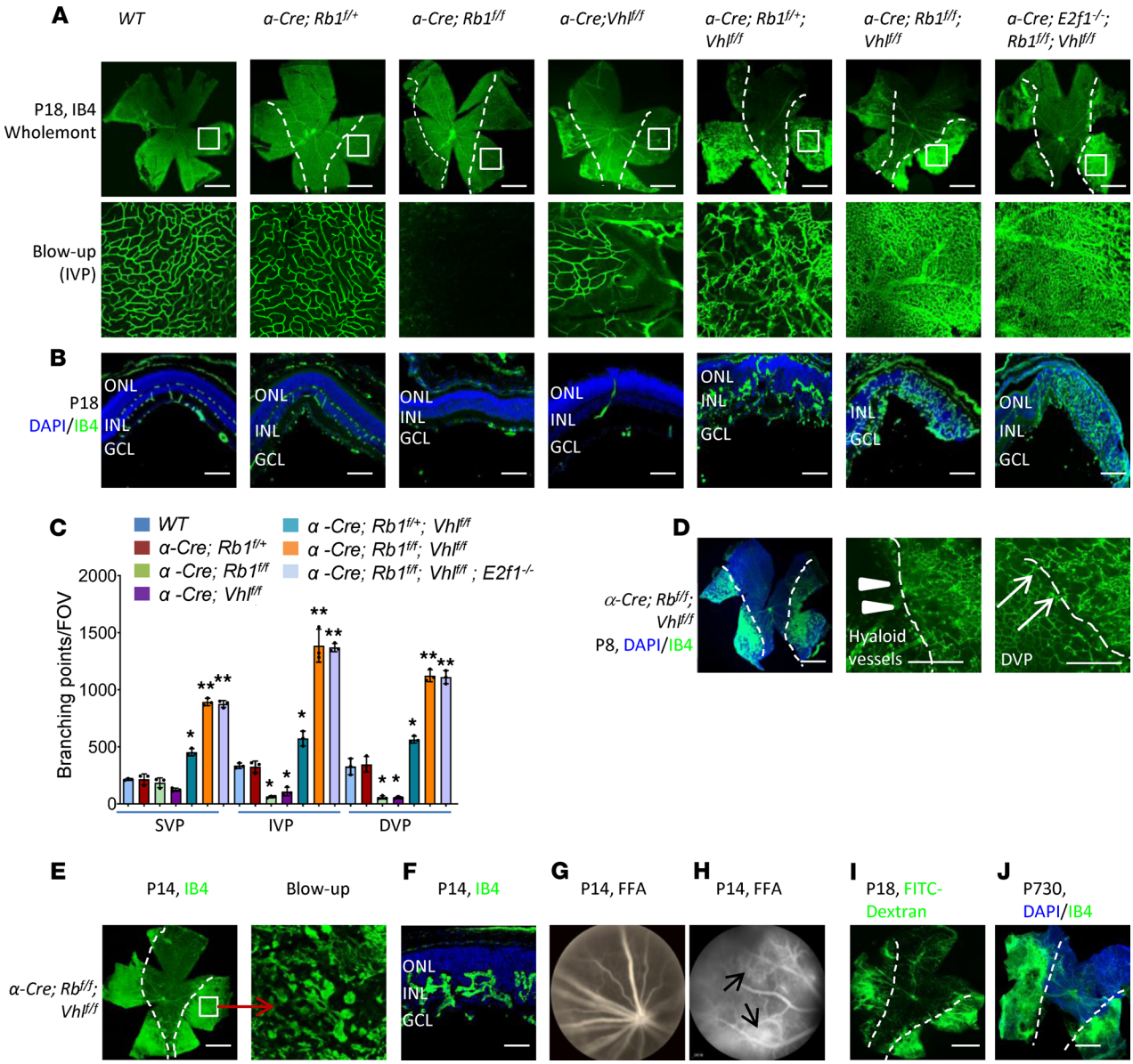

Figure 1. Retinal neovascularization in the *Rb1/Vhl*–DKO and *Rb1*$^{+/-}$ *Vhl*$^{-/-}$ retinas. (**A**) IB4 staining of P18 whole-mount retinas of indicated genotypes. Selected areas are blown up to show the vascular density. (**B**) IB4 (green) and DAPI (blue) staining of P18 retinal sections of indicated genotypes. (**C**) Quantification of vessel branching points per fields of view (FOV) by AngioTool software. (**D**) IB4 staining of the P8 *Rb1/Vhl*–DKO whole-mount retina. The hyaloid vessels and DVP layers were shown. Arrowheads indicate that new blood vessels link to hyaloid vessels. Arrows indicate new blood vessels link to retinal DVP. (**E**) IB4 staining of the P14 *Rb1/Vhl*–DKO whole-mount retina. Blowup shows the grape-like clusters of endothelial cells. (**F**) IB4 (green) and DAPI (blue) staining of the P14 *Rb1/Vhl*–DKO retinal sections shows the grape-like clusters of endothelial cells. (**G** and **H**) FFA images of the P14 *Rb1/Vhl*–DKO eye to show delayed regression of hyaloid vessels (**G**) and retinal vascular leakages (**H**, arrows). (**I**) Retinal whole-mount of P18 *Rb1/Vhl*–DKO mice after retroorbital injection of FITC-dextran, to show retinal vascular leakages. (**J**) IB4 staining of P730 (2 years old) *Rb1/Vhl*–DKO whole-mount retina. Error bars represent SD of measurements from 3 retinas (n = 3), and asterisks indicate significant differences between WT and indicated genotypes (*P < 0.05, **P < 0.01, 1-way ANOVA followed by Bonferroni's correction). The dotted lines in **A**, **D**, **E**, **I**, and **J** indicate the boundary between no Cre expression (in the center) and α-Cre expression areas (in the periphery). ONL: outer nuclear layer; INL: inner nuclear layer; IVP: intermediate vascular plexus; GCL: ganglion cell layer. Scale bars: 50 μm (**F**), 100 μm (**B**), and 200 μm (**A**, **D**, **E**, **I**, and **J**).

and Müller glia (~1.5-fold) (Figure 2, C and D, and Supplemental Figure 2). These increases paralleled increased proliferation marker protein Ki-67 (Mki67) and phospho–histone H3 (PH3) indexes in the P18-DKO retinas (Supplemental Figure 4, A and B). Although Müller cells kept dividing at P18, amacrine cells were mostly postmitotic at this point, suggesting that their slightly elevated numbers may reflect ectopic division at an early time point (Supplemental Figure 4, C and D). In summary, therefore, while deleting *Rb1* and *Vhl* modestly increases the number of 2 INL cell types, it has a profound effect on both angiogenesis and photoreceptor survival.

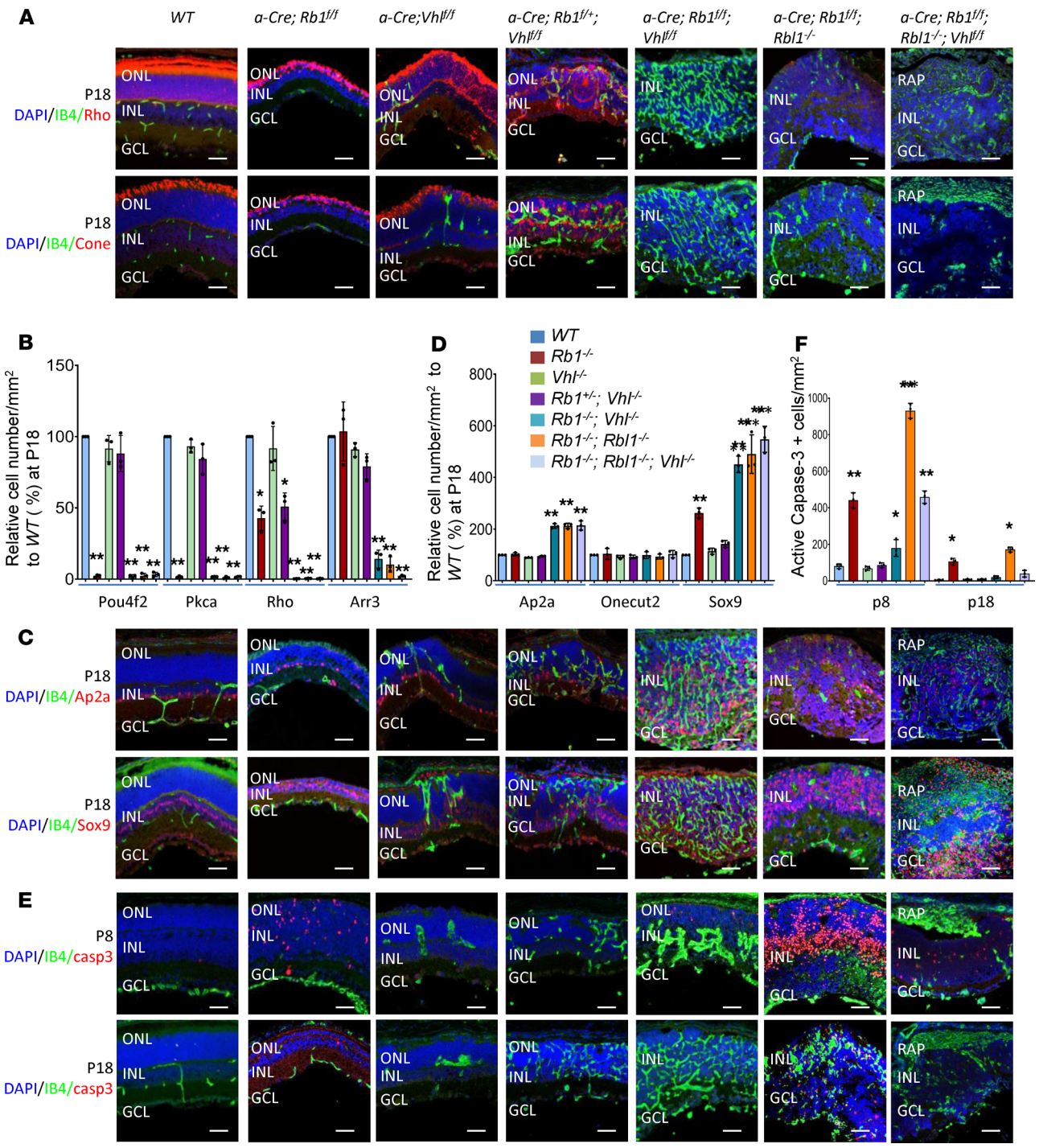

Figure 2. *Rb1* KO and *Vhl* KO are synthetically lethal to retinal photoreceptors. (**A**, **C**, and **E**) P8 or P18 horizontal retinal sections of indicated genotypes were stained for nuclear cells (DAPI, blue), vascular endothelial cells (IB4, green), rods (Rho, red, **A**), cones (Arr3, red, **A**), amacrine cells (Ap2a, red, **C**), Müller cells (Sox9, red, **C**), and apoptosis (active caspase-3, red, **E**). (**B**, **D**, and **F**) Quantification of rods, cones, bipolar cells, and ganglion cells (**B**); amacrine cells, horizontal cells, and Müller cells (**D**); and apoptosis (**F**). Error bars represent SD of measurements from 3 retinas ($n = 3$), and asterisks indicate significant differences between WT and indicated genotypes (*$P < 0.05$, **$P < 0.01$, 1-way ANOVA followed by Bonferroni's correction). RAP: Lesions of retinal angiomatous proliferation. Scale bar: 50 μm.

Rb1 binds and represses Hif target genes in the retina. A unifying explanation for the effects on angiogenesis and photoreceptor survival may be that Rb1 directly represses Hif targets in the retina. Hif can induce autophagy genes (31); thus if Rb1 indeed represses these and other Hif targets, then photoreceptor cell death in the *Rb1*/*Vhl*–null retina may be autophagic. In the *Rb1*$^{-/-}$ retina, neurons die by apoptosis (34, 44), but

notably *Rb1*/*Vhl*–DKO did not increase and instead reduced cleaved caspase-3$^+$ cells at P8 or P18 by about 2-fold (Figure 2, E and F). Western blots of P14 retinal lysates confirmed this reduction (Figure 3, A and B). Analysis of several autophagy regulators revealed that while Becn1 was not affected in the DKO retina, Atg5, Atg7, Bnip3, and Bnip3L were induced and the microtubule-associated proteins 1A/1B light chain 3B (MAP1LC3B) II/I ratio increased (Figure 3, A and B). Thus, the dramatic loss of photoreceptors in the DKO tissue is due to both autophagy and apoptosis, supporting the idea that Rb1 may repress retinal Hif targets. *Vhl*-KO alone also induced autophagy without apoptosis in the retina (Supplemental Figure 1, A and B), and likely autophagy causes the photoreceptor loss in the $Vhl^{-/-}$ retina at late stage (20, 21). One allele of *Rb1* was sufficient to suppress the expression of Atg5, Atg7, and Bnip3L in the $Vhl^{-/-}$ retina (Supplemental Figure 1, A and B), confirming Rb1 can directly inhibit Hif-induced autophagy. Indeed, $Rb1^{+/-}$ $Vhl^{-/-}$ retina had fewer rod photoreceptors than $Vhl^{-/-}$ retina (Figure 2, A and B).

To further understand why *Rb1*/*Vhl* loss induces extensive retinal angiogenesis and photoreceptor death, we performed RNA-sequencing from P14 WT, $Vhl^{-/-}$, $Rb1^{+/-}$ $Vhl^{-/-}$, and $Rb1^{-/-}$ $Vhl^{-/-}$ retinas. We analyzed differentially expressed genes (DEGs) and identified 1393 $Vhl^{-/-}$-related DEGs compared with WT. There were 820 down- and 573 upregulated genes (Supplemental Table 1). Gene list enrichment analysis indicated that the most enriched downregulated DEGs were in the pathways of ECM-receptor interaction; some photoreceptor genes were also slightly downregulated, including *Grk1*, *Slc24a1*, *Gnat1*, and *Cngb1*. The most enriched upregulated DEGs were in the pathways of ribosome biogenesis and oxidative phosphorylation, consistent with a previous report that Vhl inhibits ribosome biogenesis (45) and the vascular defects in the $Vhl^{-/-}$ retina (Figure 1, A–C). Only a few Hif pathway genes were slightly upregulated in P14 $Vhl^{-/-}$ retina, including *Nos3* and *Hmox1* (Supplemental Table 1), consistent with the presence of an inhibitor of Hif targets.

We further identified 890 $Rb1^{+/-}$ $Vhl^{-/-}$–related DEGs and 4686 DKO-related DEGs, compared with $Vhl^{-/-}$ retinas (Supplemental Table 1). For DKO retinas, the most enriched downregulated DEGs were in the pathways of oxidative phosphorylation and phototransduction; the most enriched upregulated DEGs were in the pathways of cell cycle, ECM-receptor interaction, PI3K-Akt, and Hif-1 (Figure 3, C and D). For $Rb1^{+/-}$ $Vhl^{-/-}$ retinas, the most enriched downregulated DEGs were in ribosome biogenesis, and the most enriched upregulated DEGs were in the pathways of ECM-receptor interaction, Hif-1, and PI3K-Akt. Notably, cell cycle genes were not enriched in the $Rb1^{+/-}$ $Vhl^{-/-}$ retinas (Figure 3, C and D). These RNA-sequencing data support the notion that Rb family members constrain induction of Hif-1 targets in the absence of Vhl.

Real-time PCR (RT-PCR) results supported altered expression of several Hif targets, such as *Bnip3*, *Epo*, *Tek*, *Vegfa*, and *Kdr*. Deleting *Rb1* in $Vhl^{-/-}$ retina increased expression of these genes 1.7- to 2.7-fold (Figure 3E). Deleting 1 *Rb1* allele had an intermediate effect, indicating a dose-dependent regulation of Hif target genes (Figure 3E). The changes in protein levels of Vegfa and Kdr also supported this notion (Figure 3, A and B, and Supplemental Figure 1).

To test whether Rb1 directly regulates these genes in the retina, we ran ChIP assays. It was difficult to obtain enough pure knockout material from the peripheral Cre-positive region of the *α-Cre* $Vhl^{fl/fl}$ retina; thus we assessed Rb1 binding in WT retinal explants left untreated or exposed to $CoCl_2$, which mimics hypoxia and induces Hif-1α accumulation (Supplemental Figure 5) (46). Consistent with a previous analysis in fetal liver (37), Rb1 was bound to the promoters of several Hif targets, such as *Bnip3*, *Epo*, *Kdr*, *Tek*, and *Vegfa* (Figure 3F). $CoCl_2$ treatment did not increase Rb1 binding (Figure 3F), suggesting that Hif-1α might not directly recruit Rb1 to these targets; instead and most likely, Rb1 binds E2f, which was recruited to the promoter of these targets, and recruits some cofactors that can bind and inhibit Hif protein or Hif-responsive element (37).

Dual-luciferase reporter assay using HEK293T cells indicated that Rb1 can partially repress the transcription activity of the 198-bp promoter of *Vegfa* gene (~15% reduced compared with empty vector), the 938-bp promoter of *Kdr* gene (~55% reduced compared with the empty vector), and the 337-bp promoter of *Tek* gene (~35% reduced compared with the empty vector). Rb1 did not affect the shorter 213-bp promoter of *Kdr* (Figure 3G), suggesting a requirement for upstream regions. The result with the *Vegfa* 198-bp promoter–luc reporter is consistent with results showing that E2f1 can regulate a similar reporter (47).

Together, the above genetic and molecular analyses reveal Rb1 inhibits a subset of Hif-1 target genes, providing a logical mechanism to explain why the $Vhl^{-/-}$ retina does not exhibit vessel overgrowth phenotypes, such as RAP or RCH.

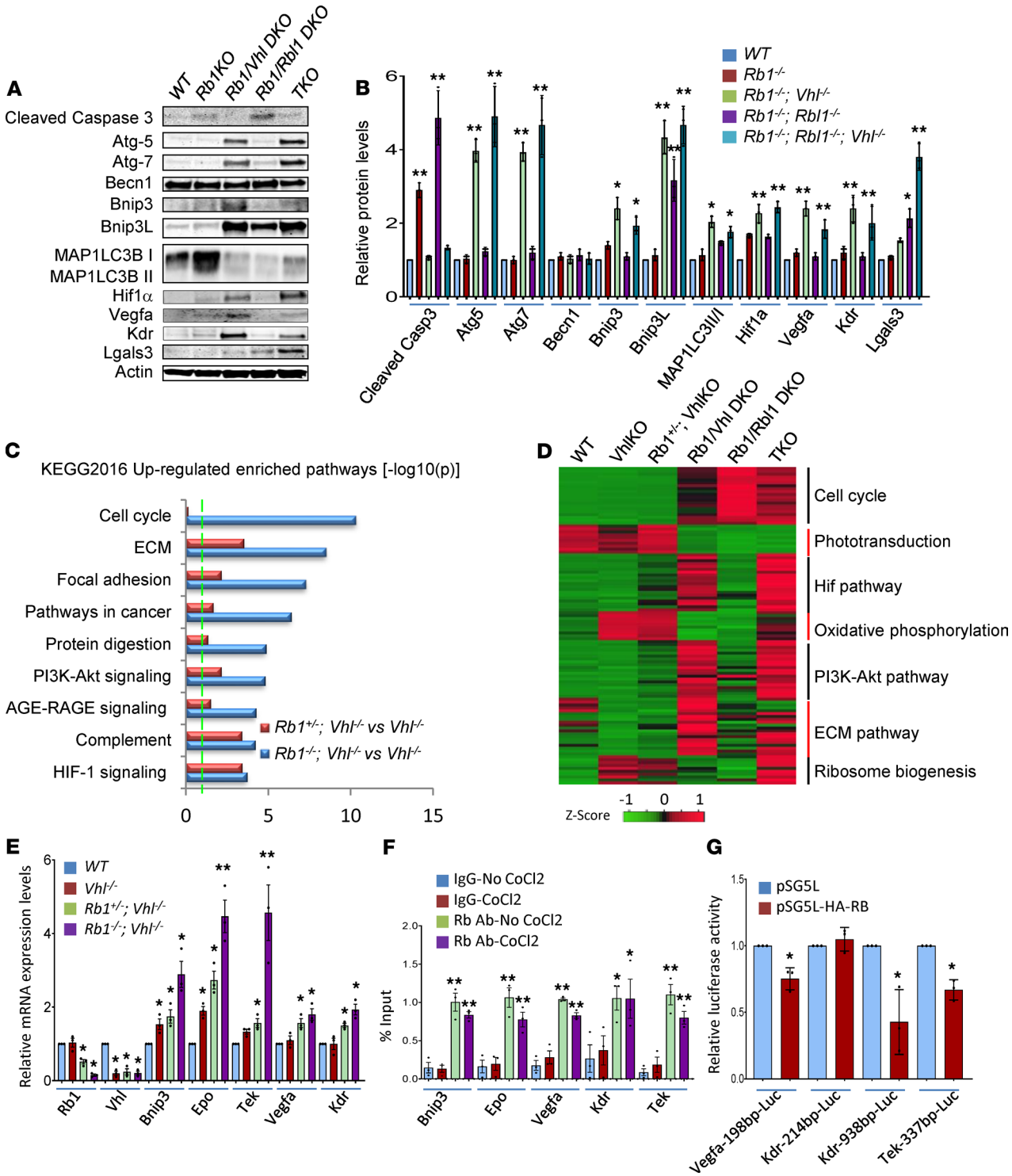

Figure 3. Rb1 directly inhibits *Vhl*-null–induced angiogenesis and autophagy. (**A**) Representative Western blots of indicated proteins in retinas of indicated genotypes. (**B**) The quantification of total protein level relative to β-actin in **A**. (**C**) Gene list enrichment analysis using Kyoto Encyclopedia of Genes (KEGG) 2016 data sets in Enrichr of *Rb1*$^{+/-}$ *Vhl*$^{-/-}$ and *Rb1/Vhl*–DKO regulated DEGs ($-\log_{10} P$). Dotted line, $P < 0.05$. (**D**) Heatmap of top 7 pathways of Vhl-, Rb1-, and Rbl1-regulated DEGs by RNA-sequencing. (**E**) The relative mRNA levels of indicated genes and indicated genotypes were analyzed by real-time PCR (RT-PCR). (**F**) ChIP using Rb1 antibody at the promoter of indicated genes and treatments in WT retinal explant cultured from P8 to P11. The enrichment of Rb1 was quantified using quantitative PCR and normalized to input. (**G**) Luciferase reporter assay. HEK293T cells were transfected with indicated luciferase reporter plasmid, and pSG5L-HA-RB or pSG5L plasmid, by Lipofectamine. Renilla luciferase plasmid was included to normalize for transfection efficiency. Error bars represent SD (**B** and **G**) or SEM (in **E** and **F**) of measurements from 3 retinas (**B**, **E**, and **F**; $n = 3$) or 3 assays (**G**; $n = 3$), and asterisks indicate significant differences between WT and indicated genotypes in **B** and **E**; or between IgG no $CoCl_2$ treatment and other indicated treatments in **F**, between pSG5L-HA-RB and pSG5L vector in **G** (*$P < 0.05$, **$P < 0.01$, 1-way ANOVA followed by Bonferroni's correction).

Rb1 suppresses the SVP in the Ccnd1$^{-/-}$ retina. To further examine the effect of Rb1 on Hif targets, we asked whether activating Rb1 represses these genes. Hif is expressed in WT retinal progenitors (21) and is required for retinal vascular development (48). There are very high levels of cyclin D1 in retinal progenitors, which activate Cdk4 and Cdk6 kinase that phosphorylate and inhibit Rb1 (41). Deleting *Ccnd1* activates Rb1, and we hypothesized that it may inhibit Hif action and impede angiogenesis in the developing retina. Indeed, *Ccnd1*$^{-/-}$ mice had retinal angiogenesis defects: There was almost no DVP or IVP, and the SVP had not reached to the peripheral retina by P18 (Figure 4, A–D).

Ccnd1 loss reduces retinal progenitor proliferation, so these vascular effects might be an indirect consequence of hypocellularity rather than Rb1-mediated repression of Hif targets, similar to the *Rd1* retinal degeneration retina (49). To examine that possibility, we took 3 approaches. First, horizontal sections of P18 *Ccnd1*$^{-/-}$ retina were stained for all 7 retinal cell types (Supplemental Figure 6). Although the retinal thickness was reduced as reported (41), clearly all retinal cell types formed and were properly laminated, excluding the possibility that neuronal developmental delay or defects caused the vascular defects.

Second, we studied the peripheral *α-Cre E2f1*$^{-/-}$ *E2f2*$^{-/-}$ *E2f3*$^{fl/fl}$ retina because removing *E2f1*, *-2*, and *-3* also reduces retinal progenitors and to an even greater extent than *Ccnd1*$^{-/-}$ (50). Notably, both SVP and DVP developed normally, although the IVP developed late (Figure 4, A–D). Thus, severe effects on the SVP and DVP are uniquely associated with *Ccnd1*$^{-/-}$ and not with hypocellularity per se.

Third, we tested directly whether suppression of angiogenesis in the *Ccnd1*$^{-/-}$ retina requires Rb1. There was no difference of body weight between *Ccnd1*$^{-/-}$ and *α-Cre Ccnd1*$^{-/-}$ *Rb1*$^{fl/fl}$ mice (Supplemental Figure 7), indicating the overall development is similar between these genotypes. The *Ccnd1/Rb1*–null retina still lacked the DVP and IVP, but strikingly, it had a completely normal SVP (Figure 4, A–D). Differentiating *Rb1*$^{-/-}$ retinal cells undergo ectopic division and some cell types die. It is unlikely that these events promote SVP development because Bax-driven cell death in the *Rb1*$^{-/-}$ retina actually impedes IVP and DVP development (40). To validate that interpretation, we further assessed the effect of *Rb1* heterozygosity, which does not perturb any aspect of retinal development (34). As with *Rb1* loss, there was a complete rescue of the SVP in the *Ccdn1*$^{-/-}$ *Rb1*$^{+/-}$ retina (Figure 4, A–D). Thus the SVP defects in *Ccdn1*$^{-/-}$ retina were caused by activated Rb1. Notably, the expression of several Hif targets was significantly repressed in *Ccnd1*$^{-/-}$ retina, which was rescued by removing 1 or 2 copies of *Rb1*, whereas only *Bnip3* was slightly reduced in the *E2f1–3*–null retina that had a normal SVP (Figure 4E). The mechanism of the DVP/IVP defects in the *Ccdn1*$^{-/-}$ retina remains unclear but may reflect inhibition of Hif-1 targets by Rb1 relatives or Rb1-independent functions of cyclin D1, such as transcriptional regulation of Notch pathway (51).

In summary, multiple genetic and molecular analyses suggest that inhibition of Rb1 by cyclin D1 in retinal progenitors is critical to permit Hif to promote normal SVP development.

Vhl is required for retinoblastoma in the Rb1/Rbl1–null retina. Because Rb1 inhibited Hif targets in the *Vhl*$^{-/-}$ retina, removing another Rb family member, such as Rbl1, might further enhance vascular overgrowth. Before addressing that hypothesis, we first asked whether Vhl affects any phenotypes caused by *Rb1/Rbl1* loss. The most striking difference between *Rb1* and *Rb1/Rbl1* loss is that only the latter causes murine retinoblastoma (34, 35). Vhl is a potent tumor suppressor in other tissues, suggesting that *Vhl* deletion might enhance retinoblastoma penetrance (13). However, whereas both Hif-1α and Hif-2α promote angiogenesis, the latter promotes while the former inhibits cancer progression (52). Notably, long-term analysis of a large cohort of mutant mice revealed that the *Rb/Rbl1/Vhl*–triple knockout (TKO) retina is resistant to retinoblastoma (Figure 5A).

All 7 retinal cell types in *Rb1/Rbl1*–DKO retina fail to exit the cell cycle and divide ectopically (34, 44). Even though there were many Mki67^{+} dividing cells at P8 and P18 (Supplemental Figure 4), they gradually exited the cell cycle when they fully developed; thus they were not tumor cells. Indeed, there were almost no Mki67^{+} cells at P138 in TKO retina (Supplemental Figure 8). These data imply predominance of Hif-1α in the cell of origin of retinoblastoma. Prior analysis of nascent tumors revealed that *Rb1/Rbl1*–null murine retinoblastoma arises from ectopically dividing amacrine cells, which have an intrinsically high resistance to apoptosis (34). Therefore, we were interested in any effects of *Vhl* loss on this lineage.

First, we assessed whether *Vhl* loss compromised the survival of the tumor cell of origin. The *Rb1/Rbl1*–null retina loses all ganglion, rod, cone, and rod bipolar cells but retains ectopically dividing amacrine, horizontal, and Müller cells (34). The TKO retina lost the same cell types as the *Rb1/Rbl1*–null tissue (Figure 2, A and B). In addition, while *Vhl* loss reduced the extent of cleaved caspase-3^{+} cells, akin to the *Rb1/Vhl*–DKO retina (Figure 2, E and F), there was increased autophagy, as Atg5, Atg7, Bnip3/Bnip3L, and the

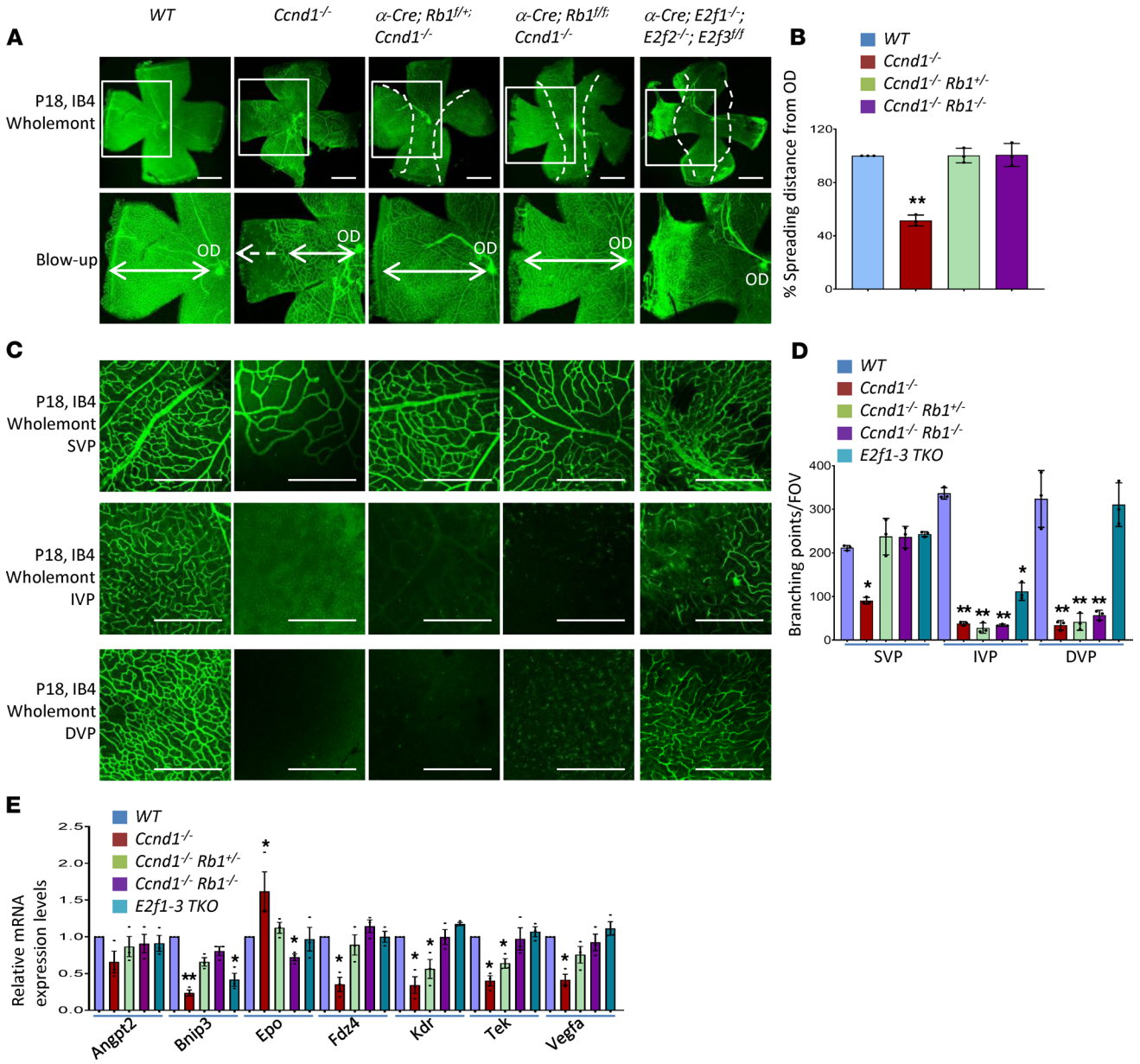

Figure 4. Hyperactive Rb1 inhibits the SVP in *Ccnd1*$^{-/-}$ retina. (**A**) IB4 staining of P18 whole-mount retinas of indicated genotypes. Selected areas are blown up to show the vascular development. Bidirectional arrows indicate the spreading distance of vascular vessels from the optic disk (OD). Dashed arrows indicate area without blood vessels. (**B**) Quantification of the spreading distance of vascular vessels from OD in **A** of indicated genotypes. (**C**) IB4 staining of the SVP, IVP, and DVP of P18 whole-mount retinas of indicated genotypes. (**D**) Quantification of vessel branching points per FOV in **C** by AngioTool software. (**E**) The relative mRNA levels of indicated genes and indicated genotypes were analyzed by RT-PCR. Error bars represent SD (**B** and **D**) or SEM (**E**) of measurements from 3 retinas ($n = 3$), and asterisks indicate significant differences between WT and indicated genotypes (*$P < 0.05$, **$P < 0.01$, 1-way ANOVA followed by Bonferroni's correction). The dotted lines in **A** indicate the boundary between no Cre expression (in the center) and α-Cre expression areas (in the periphery). Scale bar: 200 μm.

MAPLC3B II/I ratio increased (Figure 3, A and B). Notably, however, the TKO retina retained amacrine, horizontal, and Müller cells (Figure 2, C and D), indicating that Vhl is not required for the survival of the retinoblastoma cell of origin.

Indeed, there were actually more amacrine cells, and more Müller glia, when *Vhl* was missing (Figure 2, C and D). Cell-specific analysis of Mki67^{+} cells revealed that whereas both amacrine and Müller cells were dividing in the *Rb1*/*Rbl1*–null retina, by P18 Müller glia were the major dividing cell type in the TKO retina. Amacrine cells and horizontal cells were largely quiescent (Supplemental Figure 4, C and D). These features resemble the effect of *Vhl* loss in the *Rb1*$^{-/-}$ retina (Supplemental Figure 4, C and D).

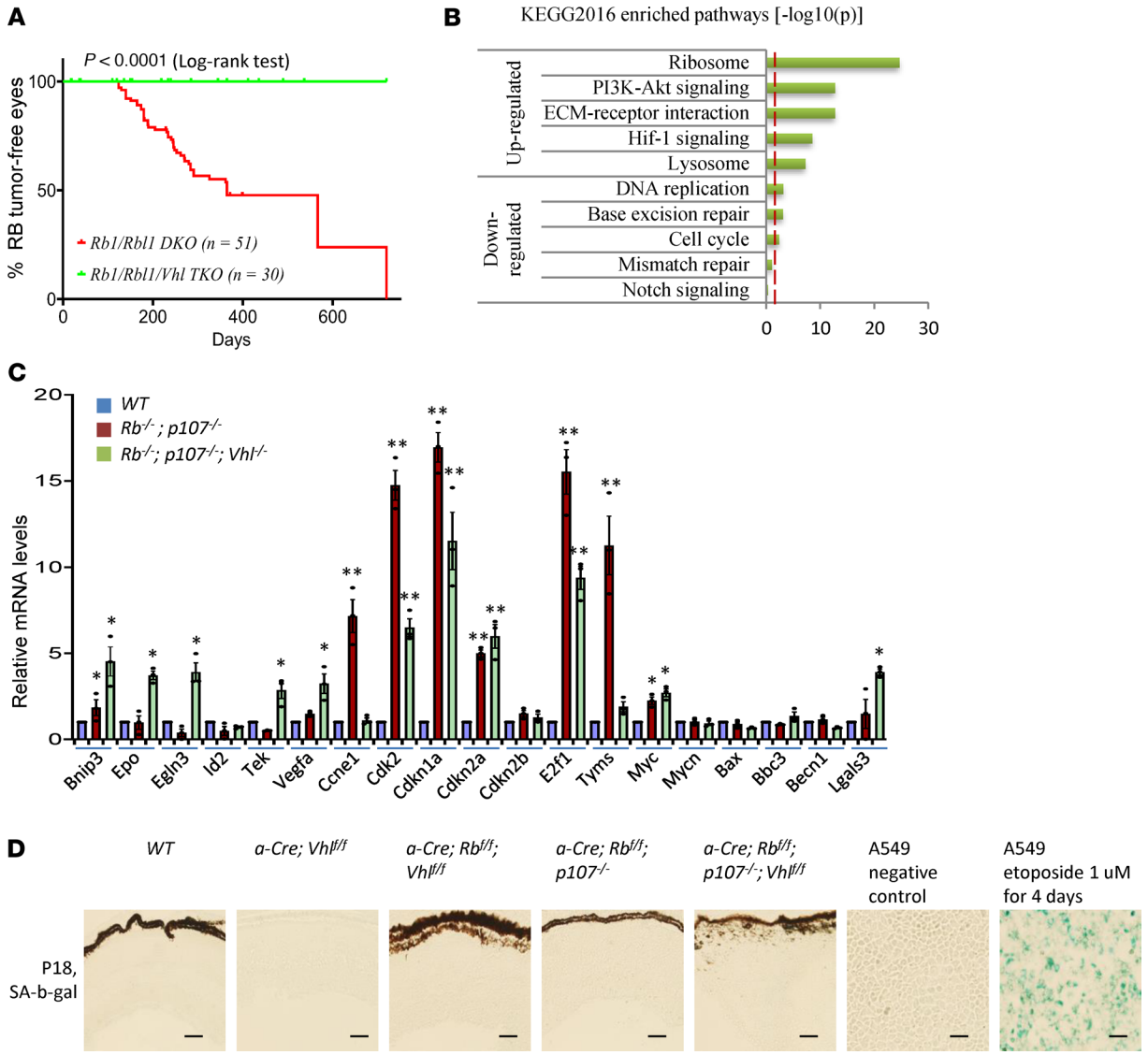

Figure 5. *Vhl* KO suppresses retinoblastoma formation in the *Rb1/Rbl1*–DKO retinas. (**A**) Kaplan-Meier (KM) curves to assess the effect of *Vhl* loss on tumorigenesis in the *Rb1/Rbl1*–DKO retina. *P* values compare the indicated genotypes (log-rank Mantel-Cox test). (**B**) Gene list enrichment analysis using KEGG 2016 data sets in Enrichr of *Rb1/Rbl1/Vhl*–TKO–regulated DEGs ($-\log_{10} P$). Dotted line, $P < 0.05$. (**C**) The relative mRNA levels of indicated genes and indicated genotypes were analyzed by RT-PCR. (**D**) P18 horizontal retinal sections of the indicated genotypes and human lung cancer A549 cells treated with (positive control) or without (negative control) etoposide were stained for senescence-associated–β-galactosidase. Error bars represent SEM of measurements from 3 retinas ($n = 3$), and asterisks indicate significant differences between WT and indicated genotypes (*$P < 0.05$, **$P < 0.01$, 1-way ANOVA followed by Bonferroni's correction). Scale bar: 200 μm (**B**).

The requirement for Vhl to maintain ectopic division in *Rb1/Rbl1*–null amacrine cells explains the absence of tumorigenesis in the TKO tissue. In line with these cellular effects, RNA-sequencing analysis identified 4077 TKO-related DEGs, compared with *Rb1/Rbl1*–DKO retinas (Supplemental Table 1). The most enriched downregulated DEGs were in the pathways of DNA replication and cell cycle; the most enriched upregulated DEGs were in the pathways of ribosome biogenesis, PI3K-Akt, ECM-receptor interaction, and Hif-1 (Figure 5B and Figure 3D). Indeed, TKO retina had lower expression of cell cycle genes, such as *Cdk2*, *Ccne1*, *E2f1*, and *Tyms*, although the expression of *Myc* family and some cell death genes (*Bax*, *Becn1*, and *Bbc3*) was similar between the 2 genotypes (Figure 5C).

Vhl loss can cause a senescent-like phenotype in mouse embryonic fibroblasts (53). However, we did not identify any signs of senescence in *Vhl*-KO, *Rb1/Vhl*–DKO, and *Rb1/Rbl1/Vhl*–TKO retinas (Figure 5D). It will be interesting to deduce how *Vhl* loss influences cell cycle gene expression, but our major goal here was to address the role of the Rb family in constraining $Vhl^{-/-}$-induced angiogenesis.

The complete absence of cancer in the TKO retina removed a confounding factor in the pursuit of this goal.

Rb1/Rbl1/Vhl-TKO retina forms RCH/RAP–like lesions. Next, therefore, we asked whether deleting *Rbl1* affects vessel growth in the *Rb1/Vhl*–null retina. Indeed, IB4 staining revealed that all 51 eyeballs of TKO mice we analyzed form RCH-like lesions after P10 (Figure 6, A and B). Human RCH generally locates at the inner retinal surface, but the RCH-like lesions described here were always in the subretinal space, resembling stage II–III RAPs (5, 6). FFA revealed subretinal vascular leakage at late stages, even though the images were not clear as the fluorescein was blocked by the persistent hyaloid vessels (Figure 6C, arrows). Histologically, the RAP lesion was a vascular mass between the neuronal retina and the RPE layer (Figure 6D). RPE cells beside RAPs often degenerated because there were many RPE vacuoles (Figure 6D, asterisks). Thus, in some areas, RAPs could penetrate the RPE layer and grow into the choroid, likely to form retinal–choroidal anastomosis (Figure 6D, arrowheads). Indeed, there were almost no RPE65$^+$ RPE cells around RAP lesions (Figure 6E). Inside the RAP lesion, similar to RCH, there were many vacuolated "foamy" stromal cells (Figure 6D, arrow), likely because *Vhl* deficiency induced abnormal lipid metabolism, as also seen in the CCRCC and liver hemangioblastoma (54). The foamy stromal cells are considered the true tumor cells in hemangioblastoma (12).

Next, we sought to define the cellular origin of the foamy stromal cells in the RAP/RCH–like lesions. They were mainly composed of Sox9$^+$ cells, without any Ap2a$^+$ amacrine cells, suggesting that they originated from Müller glia (Figure 7A). Consistent with this notion, we found that these lesions expressed high levels of Lgals3 (Figure 7A), which is expressed mainly in Sox9$^+$ Müller glial cells, but not Ap2a$^+$ amacrine or Aif1$^+$ (also called Iba1) microglial cells in WT retina (Figure 7B). Western blot and RT-PCR also confirmed this finding (Figure 3, A and B, and Figure 5C). Lgals3 is expressed in all stromal cells of human cerebellar hemangioblastoma (55). High-magnification images showed that Lgals3$^+$ cells were the stromal cells, and they never costained with IB4$^+$ endothelial cells (Figure 7A, blowup). Lgals3 also marks active microglial cells (56), but costaining with Aif1 indicated that although some microglia were present, most cells in the RAP lesions were Aif1$^-$, further supporting a Müller glia origin (Figure 7A).

RPE cells also express Sox9 (57); thus it was possible that RPE cells are the cellular origin of the RAP lesions. However, 4 findings countered this idea. First, there were almost no RPE65$^+$ cells in RAP lesions (Figure 6E). Second, RPE cells did not express Lgals3 (Figure 7B, arrow). Third, laser capture of microdissected RAP lesions followed by PCR analysis of genomic DNA confirmed Cre-mediated recombination of *Rb1* in the RAP lesions, confirming the retinal origin of the lesions (260-bp band in Figure 7C). Some un-recombined bands (670 bp) may derive from blood vascular cells. Finally, we used Z/Red Cre-indicator mice to lineage-trace knockout cells (58) and found many DsRed$^+$ cells in the RAP lesions, indicating that the cell of origin derives from the Cre-expressing retinal cells (Figure 7D). Thus, deleting *Vhl* in the *Rb1/Rbl1*–null retina prevented amacrine cell transformation but induced RCH/RAP–like lesions that originate from Müller glial cells.

Discussion

The *Vhl*$^{-/-}$ retina does not exhibit vascular overgrowth, such as RAP or RCH (20, 21), but it is unclear how Hif target expression is suppressed. Our data now pinpoint Rb1 as the critical angiogenic inhibitor. Thus, the *Rb1/Vhl*–DKO retina exhibits striking levels of angiogenesis. Multiple pieces of evidence argue that this is not an indirect consequence of other cellular effects of *Rb1* loss. First, Bax-driven apoptosis in the *Rb1*$^{-/-}$ retina actually impedes vessel growth (40). Second, *Rb1* heterozygosity does not perturb retinal development (34) but stimulates vessel growth in the *Vhl*$^{-/-}$ retina. Third, deleting *E2f1* completely rescues ectopic division, apoptosis, and abnormal lamination in the *Rb1*$^{-/-}$ retina (40), yet it does not reduce the excessive vessel growth in the DKO retina. Fourth, Hif can also stimulate autophagy, and removing *Rb1* and *Vhl* triggers autophagic death of photoreceptors. Fifth, deleting *Rb1* induces several Hif targets that drive both angiogenesis and autophagy. Finally, ChIP assays show that Rb1 protein binds to the promoters of several Hif targets in vivo, and reporter assays indicated that Rb1 could partially inhibit their transcription. Together, these data present a strong case that Rb1 directly inhibits Hif target expression in the retina and explains why vascular growth is constrained in the *Vhl*$^{-/-}$ murine tissue. In addition, activating Rb1 in *Ccnd1*$^{-/-}$ retina suppresses Hif target expression and impedes SVP development, suggesting that Rb1 is necessary and sufficient to suppress Hif targets.

Our data indicate that in the *Vhl*$^{-/-}$ retina, *Rb1* is haploinsufficient with respect to blocking either angiogenesis or autophagy. This finding is intriguing given that the *Rb1*$^{+/-}$ retina is normal (34). *Rb1* is one of the classical tumor suppressor genes, which are thought to require mutation or loss of both alleles to facilitate tumor progression (59). However, it has become clear that haploinsufficiency may contribute to

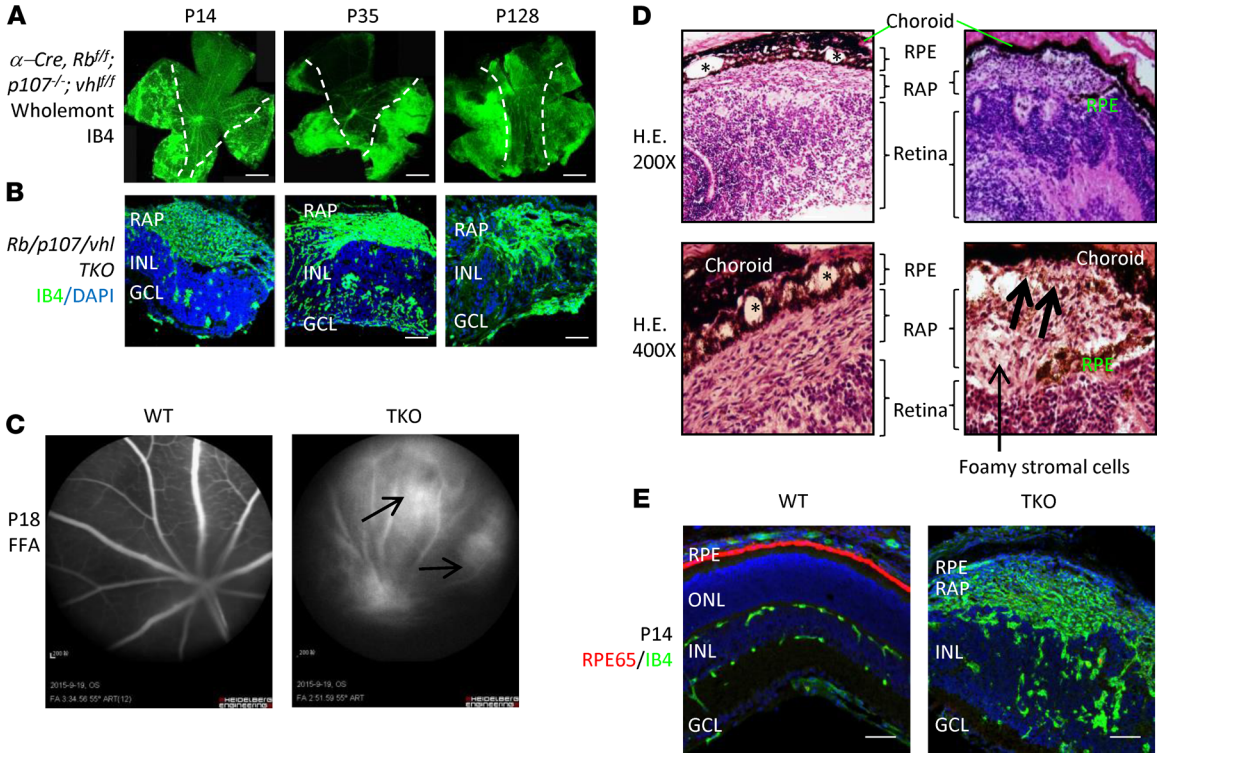

Figure 6. *Rb1/Rbl1/Vhl* TKO induces RCH-like and RAP-like lesions. (**A**) IB4 staining of *Rb1/Rbl1/Vhl*–TKO whole-mount retinas of indicated ages. (**B**) Horizontal sections of *Rb1/Rbl1/Vhl*–TKO retinas of indicated ages were stained for nuclear cells (DAPI, blue) and vascular endothelial cells (IB4, green). (**C**) FFA images of P18 WT or *Rb1/Rbl1/Vhl*–TKO retinas. Arrow indicates the vascular leakages from the subretinal RAP-like lesion. (**D**) H&E staining of the RAP lesions. The 2 big arrows indicate that RAP invades into the sub-RPE space. (**E**) P14 horizontal sections of WT and *Rb1/Rbl1/Vhl*–TKO retinas were stained for nuclear cells (DAPI, blue), vascular endothelial cells (IB4, green), and RPE cells (RPE65, red). The dotted lines in **A** indicate the boundary between no Cre expression (in the center) and α-Cre expression areas (in the periphery). Scale bar: 50 μm.

tumorigenesis without loss of heterozygosity, such as is the case for *Brca1*, *Brca2*, and *Tp53* (59). *Rb1* haploinsufficiency has been associated with increased genomic instability in premalignant osteoblasts (60) and fibroblasts (61). Potentially, therefore, some of the phenotypes in patients with VHL might be related to partial reduction in *Rb1* levels.

We find that *Vhl* loss induces retinal autophagy, which is the likely reason for delayed, partial loss of photoreceptors in the $Vhl^{-/-}$ retina (20, 21). *Rb1* or *Rb/Rbl1* loss triggers apoptosis of certain retinal neurons (34, 35), but we find that *Vhl* loss partially suppresses apoptosis in the $Rb1^{-/-}$ and *Rb1/Rbl1*–null retina. This suppression may be linked to enhanced autophagy (62). Our data suggest that the combination of residual apoptosis plus enhanced autophagy contributes to synthetic lethality in *Rb1/Vhl*–DKO rods and cones. It is also intriguing that inhibitory neurons and Müller glia can escape apoptosis or autophagy, but excitatory neurons die in both conditions. This finding has important implications in understanding the pathogenesis of retinal diseases. They have common risk factors, such as smoking, which can inactivate *Rb1* (63), and oxidative stress, which can activate autophagy (64). In addition, although *Vhl* loss can induce cell cycle arrest of *Rb1*-null or *Rb1/Rbl1*–null amacrine cells, it seems to enhance division in the Müller glia. This could contribute to reactive gliosis in some vascular retinal diseases.

Although *Vhl* is a well-known tumor suppressor, its deletion completely suppresses retinoblastoma in the *Rb1/Rbl1*–null retina. These tumors arise from ectopically dividing amacrine cells (34), so the quiescence of *Rb1/Rbl1/Vhl*–null amacrine cells as early as P18 provides a logical explanation for tumor suppression. Although both Hif-1α and Hif-2α are stabilized in *Vhl*-null retina, Hif-1α is the major mediator of retinal phenotypes (20, 21). In many instances Hif-1α acts as a tumor suppressor while Hif-2α promotes tumor progression (52). For example, Hif-2α, rather than Hif-1α, is the key driver of renal cancer progression (65). Thus, it is possible Hif-1α inhibits retinoblastoma initiation in the *Rb1/Rbl1*–null retina.

The absence of cancer in the *Rb1/Rbl1/Vhl*–TKO retina was an advantage because it meant that any new vascular phenotypes relative to the TKO tissue could not be an indirect consequence of tumorigenesis.

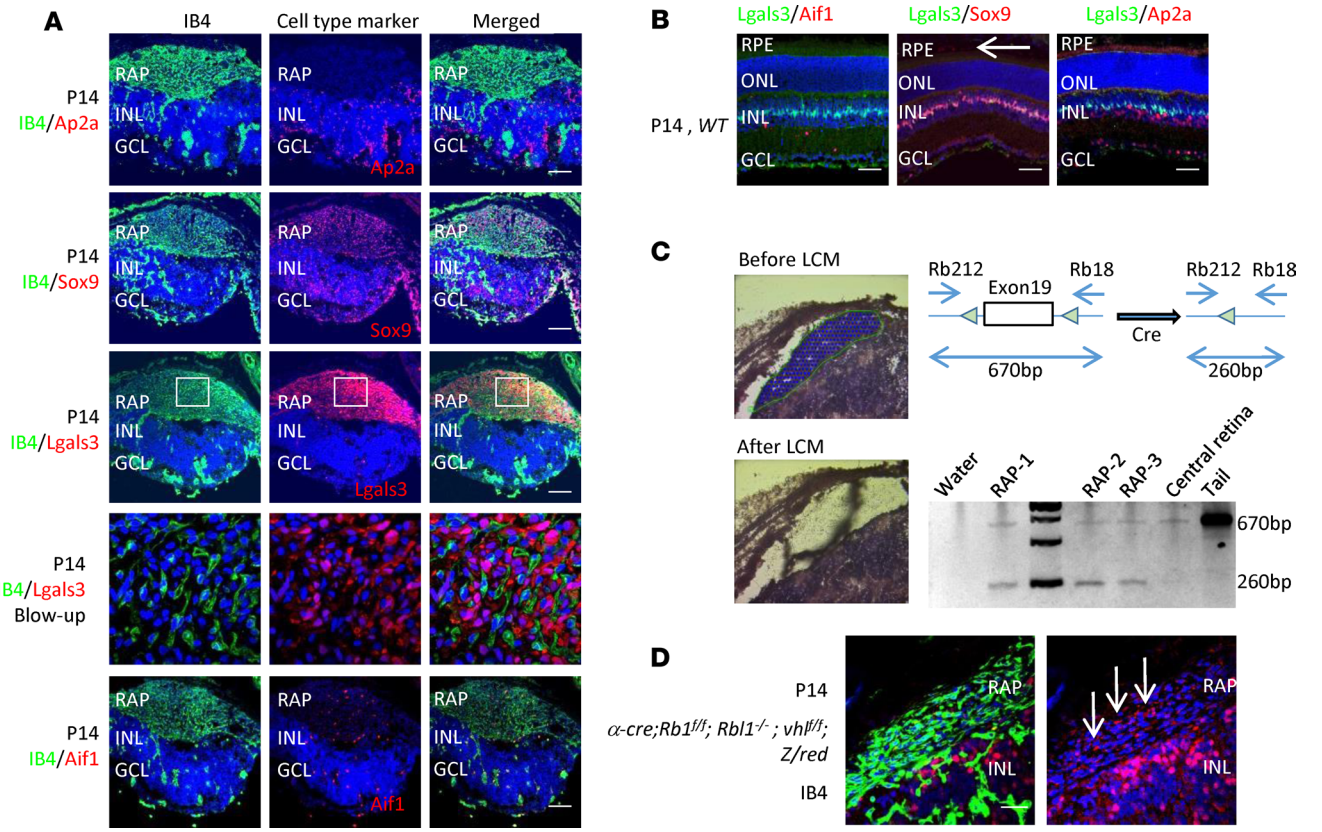

Figure 7. The cellular composition of the RCH-like and RAP-like lesions in the *Rb1/Rbl1/Vhl*–TKO retina. (**A**) P14 horizontal TKO retinal sections were stained for nuclear cells (DAPI, blue), vascular endothelial cells (IB4, green), amacrine cells (Ap2a, red), Müller cells (Sox9, red), Müller/microglial cells (Lgals3, red), and microglial cells (Aif1, red). Blowup shows that Lgals3$^+$ cells are stromal cells but not IB4$^+$ vascular endothelial cells. (**B**) P14 horizontal WT retinal sections were stained for nuclear cells (DAPI, blue), Müller/microglial cells (Lgals3, green), amacrine cells (Ap2a, red), Müller cells (Sox9, red), and microglial cells (Aif1, red). Arrow indicates RPE cells also express low levels of Sox9 but not Lgals3. (**C**) Genomic DNA extracted from the laser capture microdissected (LCM) RAP lesions on slides were amplified by PCR for the floxed alleles of exon 19 of *Rb1* gene. Primers are Rb212 and Rb18. The 670-bp band represents the un-recombined allele; 260-bp band represents recombined allele. (**D**) P14 horizontal (*α-Cre*, *Rb1$^{fl/fl}$*, *Rbl1$^{-/-}$*, *Vhl$^{fl/fl}$*, and *Z/red*) retinal sections were stained for nuclear cells (DAPI, blue), vascular endothelial cells (IB4, green), and DsRed (red). Arrows indicate some representative DsRed$^+$ or α-Cre-expressing cells in the RAP-like lesion. Scale bar: 50 μm.

Deleting all 3 genes generated a mouse model with subretinal RCH- or RAP-like lesions. *Scl-Cre^{ER}*–induced *Vhl* deletion in hemangioblasts can generate some features of early-stage RCH; however, histologically there are no hemangioblastoma structures and neovascularization in the retina, except some foamy stromal cell clusters (27). *Vhl* loss alone does not induce kidney VHL disease, but *Rb1/p53/Vhl* TKO induces a CCRCC mouse model (29). Similarly, our results show that the RCH-like lesions can originate from retinal cells, but *Vhl* loss alone may not be sufficient. The foamy cells in the RCH-like lesions we detected originated from Müller glia, which express high levels of Sox9. Consistent with a report that Lgals3 is a diagnostic marker for brain hemangioblastoma (55), we found RCH-like lesions express Lgals3, indicating that it is also a possible biomarker for diagnosing human RCH. Because most eyes of RCH patients do not need to be enucleated, it has remained unclear whether human RCH has a glial component. An early study referred to an astrocytic component of RCH (17). More recently, using histological, immunohistochemical, and ultrastructural methods to study 3 cases where samples were available, 2 groups reported that GFAP$^+$ glial cells are a major component of human RCH (18, 19). The cell of origin of human RCH needs further investigation, but our work supports the notion that foamy stromal cells may originate from Müller glia.

The RCH/RAP–like lesions are located in the subretinal space and can induce degeneration of the RPE and invade into choroid. These features are similar to advanced stage III human RAP. Early-stage RAP is observed in several mouse mutants, including mice with ONL-specific Vegf overexpression (7) or inactivation of *Vldlr* (9) or *Srf* (10) and in *Bst*-mutant (8) and *NRV2*-mutant mice (11). The retinal neovascularization in these mice is similar to stage I–II RAPs and may be related to local Vegf upregulation.

However, there are no obvious stromal cells, and no angiomatous complexes in the later stages, which are quite different from the pathological changes in late-stage human RAP (5, 6). For the same reasons as RCH, few reports have described the cellular features of human RAP. Recent studies found that RAP is a circumscribed intraretinal angiomatous complex within the outer part of the neurosensory retina, composed of endothelial cells and stromal cells. Endothelial cells within the RAP lesion stained positively for vWF and VEGF (5, 6). However, retinal cell markers (neuronal or glial) were not stained in the RAP lesion; thus it remains unclear whether there is a glial component. Our work suggests that glia is a major component of RAP-like structures in mice. Based on these data, it will be interesting for the field to revisit the question of the origin of stromal cells in human RAP.

In summary, our work exposes previously unrecognized roles for the Rb family in constraining retinal angiogenesis and autophagy and establishes a potentially new mouse model of RCH/RAP, which will be a useful tool in dissecting the pathogenesis of these disorders, optimizing therapeutic strategies, and stimulating further work to address the origins of stromal cells in the human disease.

Methods

Mouse strains and genotyping. Mice were treated according to institutional and national guidelines. All procedures were performed in compliance with the Association for Research in Vision and Ophthalmology (ARVO) statement for the use of animals in ophthalmic and visual research. *α-Cre* mice (P. Gruss, Max Planck Institute for Biophysical Chemistry, Göttingen, Germany), *Ccnd1*$^{-/-}$ mice (The Jackson Laboratory, stock 002935), *E2f1*$^{-/-}$ mice (M. Greenberg, Harvard Medical School, Boston, Massachusetts, USA), *E2f2*$^{-/-}$ mice (G. Leone, The Ohio State University, Columbus, Ohio, USA), *E2f3*$^{fl/fl}$ mice (G. Leone), *Rb1*$^{fl/fl}$ mice (A. Berns, the Netherlands Cancer Institute, Plesmanlaan, Amsterdam, the Netherlands), *Rbl1*$^{-/-}$ (*p107*$^{-/-}$) mice (M. Rudnicki, University of Ottawa, Ottawa, Ontario, Canada), *Vhl*$^{fl/fl}$ mice (The Jackson Laboratory, stock 004081), and *Z/Red* mice (The Jackson Laboratory, stock 005438) were maintained on a mixed background. Different genotypes were compared within the same litter and across at least 3 litters. We have not noted any phenotypic differences in separate litters. Genotyping was performed as before and as per The Jackson Laboratory guideline.

Histology, immunofluorescence, and measurements. Eyeballs were fixed for 1 hour at 4°C in 4% paraformaldehyde, embedded in OCT (Tissue-Tek 4583), frozen on dry ice, and cut into 12- to 14-μm sections on Superfrost slides. The following antibodies were used: Aif1 (Wako 019-19741), Ap2a (Santa Cruz Biotechnology SC-8975), Calb1 (MilliporeSigma C9848), cleaved caspase-3 (Cell Signaling Technology 9661), Arr3 (MilliporeSigma AB15282), Crx (C.Y. Gregory-Evans, Imperial College School of Medicine, London, United Kingdom) (66), DsRed (Clontech 632496), Glul (MilliporeSigma MAB302), Lgals3 (Santa Cruz Biotechnology SC-19283), Mki67 (BD Pharmingen 550609), Onecut2 (R&D Systems AF6294), Pax6 (DSHB AB-528427), PH3 (Santa Cruz Biotechnology SC-8656), Pou4f2 (Santa Cruz Biotechnology SC-6062), PKC-α (MilliporeSigma P5704), rhodopsin (Santa Cruz Biotechnology SC-57433), RPE65 (Abcam ab13826), Sox9 (MilliporeSigma AB5535), and Thrb2 (D. Forrest, NIH) (67). Vascular endothelial cells were labeled by FITC-conjugated IB4 (MilliporeSigma L2895). Antigen retrieval was performed as described (44). Primary antibodies or labeled cells were visualized using donkey anti-mouse, donkey anti-rabbit, and donkey anti-goat antibodies conjugated with Alexa Fluor 488, Alexa Fluor 568, or Alexa Fluor 647 (1:1000; Molecular Probes, Thermo Fisher Scientific). Nuclei were counterstained with DAPI (MilliporeSigma D9542) and mounted with Mowiol (MilliporeSigma 81381). Validations of the primary antibodies are provided on the manufacturers' websites or in the referenced citations.

For whole-mount staining, eyeballs were enucleated and incubated for 30 minutes in 4% paraformaldehyde. The retinas were incubated at 4°C with FITC-conjugated IB4 (MilliporeSigma L2895) and DAPI in PBS for 1–2 days. After brief washes with PBS, radial cuts were made to divide the retina into 4 quadrants to flatten the retina, and flat retinas were mounted with Mowiol.

Stained sections and slides were analyzed using a Zeiss Axio Imager Z2 fluorescence microscope and Nikon C1si confocal microscope. ImageJ (NIH) was used for cell counting. The positive cells of active caspase-3, Mki67, PH3, and cell type markers were counted manually. For vascular blood vessel analysis, representative images were analyzed using the AngioTool (National Cancer Institute) to assess the density of the vascular plexus. In brief, at least three ×200 magnification images (320 × 320 μm FOV per retina) per eye and 3 eyes from the same genotypes of different litters were counted. To compare the vascular density

of the *Rb1/Vhl*–DKO retina to other genotypes, we used vascular images taken from a similar depth below the GCL to represent the IVP and DVP for the *Rb1/Vhl*–DKO retina.

To generate 3D images for retinal vasculature, 40 *Z*-stack images were taken using a Nikon C1si confocal microscope, and ImageJ was used to convert these *Z*-stack images into a 3D video.

Senescence-associated β-galactosidase staining. Human lung cancer A549 cells (ATCC CCL-185) on coverslips (with or without pretreatment of etoposide 1 μM for 4 days) and frozen horizontal retinal sections were stained for β-galactosidase at pH 6.0 using the senescence-associated β-galactosidase staining kit (Cell Signaling Technology 9860). Color images were taken using an Olympus BX61 microscope. For each genotype, at least 3 retinas were analyzed.

H&E staining for frozen sections. Slides were rinsed once with 1× PBS, then stained with Mayer's hematoxylin for 5 minutes. They were then rinsed with running tap water for 4 minutes, dehydrated to 95% ethanol by dipping for 10–20 seconds in alcoholic eosin, and then dehydrated through at least 2 more changes of 95% ethanol and 100% ethanol. They were then cleared through 3 changes of xylene and mounted on coverslips with Permount (Thermo Fisher Scientific SP15-100). Color images were taken using an Olympus BX61 microscope.

RNA extraction, reverse transcription, and quantitative real-time PCR. Total RNA was isolated from peripheral retinas (α-Cre expression area) using TRIzol reagent (Invitrogen, Thermo Fisher Scientific) or RNeasy Mini Kit (Qiagen) followed by digestion with RNAse-free DNAse (DNA-free, Invitrogen, Thermo Fisher Scientific) to remove DNA contamination. After quantification by a NanoDrop (NanoDrop Technologies), first-strand cDNA was synthesized from 0.2 to 1.0 μg of total RNA using the RT Reagent Kit with gDNA Eraser (TaKaRa) or SuperScript II first-strand synthesis system (Invitrogen, Thermo Fisher Scientific). PCR primers are listed in Supplemental Table 2. Real-time quantitative PCR was performed using the qTOWER 2.2 PCR machine (Analytik Jena) or C1000 touch Thermal Cycler (Bio-Rad). Tests were run in duplicate on 3 separate biological samples with EvaGreen PCR Supermix (SsoFast, Bio-Rad) or SYBR Green PCR Master Mix (Applied Biosystems, Thermo Fisher Scientific). PCR consisted of 40 cycles of denaturation at 95°C for 15 seconds and annealing and extension at 55°C for 30 seconds. An additional cycle (95°C, 15 seconds) generated a dissociation curve to confirm a single product. Values obtained for test RNAs were normalized to β-actin mRNA levels.

RNA-sequencing. Total RNAs were extracted from dissected α-Cre–expressing peripheral retinas using TRIzol (Invitrogen, Thermo Fisher Scientific) and treated with RNAse-free DNAse I (New England Biolabs) to remove genomic DNA. The yield of total RNA was assessed using NanoDrop (Thermo Fisher Scientific). The cDNA libraries were prepared using an Illumina TruSeq RNA sample preparation kit, and the quality was assessed using an Agilent 2100 Bioanalyzer (Agilent Technologies). For sequencing, the cDNA libraries were loaded on an Illumina HiSeq 2500 at Biomaker (Beijing, China). The raw sequence reads in FASTQ format were processed and analyzed as previously reported (68, 69). Briefly, the sequencing quality was first assessed using FastQC, and poor-quality 5′ end reads were trimmed using a Perl script and then mapped onto mouse genome (mm9) using TopHat2, allowing for up to 2 mismatches as default settings. Reads that were mapped onto multiple genomic locations were discarded, and a custom R script was used to calculate the reads per kilobase million (RPKM) of each gene and obtain the expression profile of each sample. The expression fold change of each coding gene of mutated retinas (including $Vhl^{-/-}$, $Rb1^{+/-}$ $Vhl^{-/-}$, *Rb1/Vhl*–DKO, *Rb1/Rbl1*–DKO, and *Rb1/Rbl1/Vhl*–TKO) retina compared with WT retina was calculated using the following formula: Fold change = $(RPKM + 1)^{mutated}$ / $(RPKM + 1)^{WT}$. The genes for which expression fold changes were greater than 1.54 or less than 0.65 were selected as the mutated related DEGs. The heatmap was generated using Heatmapper (70). The function enrichment of DEGs was performed using Enrichr (71, 72); the pathways with adjusted *P* value less than 0.05 were chosen to report.

Ex vivo retinal explant cultures and ChIP. Retinal explants obtained from P8 WT C57/BL mice were cultured using a modified protocol from previously described methods (73, 74). Briefly, both eyes were enucleated and retinas were carefully peeled away from the RPE, and radial cuts were made to flatten the retina. The flattened retina was transferred to the membrane of a Millicell insert (MilliporeSigma, PICM03050) with the photoreceptors facing down. The insert was placed into the wells of a 6-well plate (Costar 3516, Corning); each contained 1300 μL of retinal explant media, which was replaced every 2 days and was maintained in a 37°C incubator with 5% CO_2 for 3 days. The retinal explant basal medium was serum-free and made from Neurobasal A, DMEM/F12 medium, and N2/B27 supplements (Life Technologies). Cultured explants were exposed to 300 μM $CoCl_2$ (MilliporeSigma) treatment or kept as PBS-treated controls. The ChIP assay was performed using Magna ChIP A/G Chromatin Immunoprecipitation Kit (Millipore Temecula) according to the manufacturer's instructions. Briefly, retinal explants treated with or without $CoCl_2$ were

cut into small pieces and then cross-linked for 20 minutes by addition of formaldehyde to a final concentration of 1%. The cross-linking was stopped by adding 1/20 volume of 2.5 M glycine and lysed by SDS lysis buffer. Then cell lysate was sonicated and immunoprecipitated with antibodies specific to Rb1 (1:100, Cell Signaling Technology, 9309) or negative control IgG. After protein/DNA complexes were eluted, reverse cross-linked to free DNA, and purified, the specific DNA fragments were quantified using real-time PCR and normalized to input from the same sample. The primer sequences for the promoters analyzed are provided in Supplemental Table 3.

Plasmid construction and reporter assays. pREP4-Luc vector was from K. Zhao (NIH) (75). A 445-bp mouse DNA fragment from –198 to +247 around *Vegfa* transcriptional start site (TSS) was amplified using the primers Vegfa–p500-f1 and Vegfa–p500-r1; a 402-bp mouse DNA fragment from –213 to +189 around *Kdr* TSS was amplified using the primers Vegfr2–p400-f1 and Vegfr2–p400-r1; a 1127-bp mouse DNA fragment from –938 to +189 around *Kdr* TSS was amplified using the primers Kdrf 1127 and Vegfr2–p400-r1; a 597-bp DNA fragment from –337 to +260 around *Tek* TSS was amplified using the primers Tie2–p500-f1 and Tie2–p500-r1. The sequences of the abovementioned primers are as follows: Vegfa–p500-f1 (5′-CCCGGTACCgtttgaaggggtgcacagat-3′, KpnI site underlined); Vegfa–p500-r1 (5′-GGCAAGCTTAACCGTTGGCACGATTTAAG-3′, HindIII site underlined); Vegfr2–p400-f1 (5′-CCCGGTACCttgctctcagatgcgacttg-3′, KpnI site underlined); Vegfr2–p400-r1 (5′-GGCAAGCTTAAGTCACAGAGGCGGTATGC-3′, HindIII site underlined); Kdrf 1127 (5′-CCCGGTACCaccggtttcctctttgttcc-3′, KpnI site underlined); Tie2–p500-f1 (5′-CCCGGTACCgctgagagctgacctcaacc-3′, KpnI site underlined); and Tie2–p500-r1 (5′-GGCAAGCTTATGGTCCACTCGCTCTTGTT-3′, HindIII site underlined).

The amplified DNA fragments were digested with KpnI and HindIII, ligated to KpnI/HindIII–digested pREP4-Luc to generate Vegfa-198bp-Luc, Kdr 213bp-luc, Kdr 938bp-luc, and Tek-337bp-luc. The inserts were confirmed by DNA sequencing. pSG5L-HA-RB and pSG5L vectors were from William Sellers (Broad Institute, Cambridge, Massachusetts, USA) (76). HEK293T cells (ATCC CRL-11268) were transfected with the pREP4-Luc vectors and the pSG5L-HA-RB or pSG5L vectors using Lipofectamine 2000 (Invitrogen, Thermo Fisher Scientific). In transient assays, 0.01 μg of renilla Luc plasmid was included to normalize transfection efficiency. Dual-luciferase assays were performed using Dual-Luciferase Reporter Assay system (Promega E1901) as described (77).

Laser capture and recombined PCR of floxed Rb1 gene. RAP lesions were dissected from 10-μm H&E sections using the Zeiss PALM MicroBeam system and captured into a tube with 10 μL of the buffer (1 mM EDTA; 20 mM Tris [pH 8]) containing 2 mg/mL proteinase K. Cells were incubated at 55°C overnight in 10 μL of capture buffer followed by heat inactivation of proteinase K at 99°C for 10 minutes. Two microliters of the buffer was used for each PCR. The PCR primers were Rb18 (5′-GGCGTGTGCATCAATG-3′) and Rb212 (5′-GAAAGGAAAGTCAGGGACATTGGG-3′).

Western blotting. Peripheral retinas were homogenized with a 30-gauge needle 5–10 times in 1× cell lysis buffer (Cell Signaling Technology 9803) with 0.1 mM PMSF, 1 μg/mL aprotinin, and 1 μg/mL leupeptin. Proteins were separated by SDS-PAGE, transferred to nitrocellulose or PVDF membranes, and analyzed using ODYSSEY Infrared Imaging System (LI-COR) with antibodies against active caspase-3 (Cell Signaling Technology 9661), Atg5 (Santa Cruz Biotechnology SC-33210), Atg7 (Santa Cruz Biotechnology SC-33211), Becn1 (Cell Signaling Technology 3495S), Bnip3 (Cell Signaling Technology 3769), Bnip3L (Santa Cruz Biotechnology SC-28240), Hif-1α (MilliporeSigma 04-1006), Kdr (MilliporeSigma 07-716-1), Lgals3 (Santa Cruz Biotechnology SC-19283), MAP1LC3B (Cell Signaling Technology 2775), Vegfa (Santa Cruz Biotechnology SC-507), and β-actin (MilliporeSigma A5441).

Retroorbital injection of FITC-dextran. FITC-dextran (MilliporeSigma FD2000S) was dissolved in double-distilled H_2O at a concentration of 50 mg/mL, centrifuged at 10,000 *g* for 5 minutes, and collected as the supernatant. P18 mice were anesthetized with an intraperitoneal (IP) injection of 4.6% chloral hydrate (2.5 mL/kg). Then, 0.15 mL of FITC-dextran was injected into the lateral canthus of the left orbit using a 1-mL syringe and 30-gauge needle. Eyeballs were enucleated 1 minute after the injection. Retinal whole mounts were prepared and flattened with a coverslip and were photographed with Zeiss Axio Imager Z2 fluorescence microscope.

FFA. Fluorescein angiography was performed using a Micron III retinal imaging system or Heidelberg retina angiograph system. P14–P18 mice were anesthetized with an IP injection of 4.6% chloral hydrate (2.5 mL/kg), and the pupils were dilated by 0.1% tropicamide solution. Fluorescein images were captured at different time points after IP injection of 0.1 mL of 2% fluorescein sodium (Novartis).

Statistics. All data were presented as mean ± SD or mean ± SEM. KM survival curves were created and statistical analysis was performed using GraphPad Prism software (GraphPad Software). The results were analyzed by 1-way ANOVA followed by Bonferroni's correction for multiple comparisons and 2-tailed Student's *t* test for comparisons between 2 groups. The *P* value of KM curves was calculated by log-rank (Mantel-Cox) test.

Study approval. All animal procedures were reviewed and approved by the Ethical Review Committee of Animal Research of West China Hospital, Sichuan University, Chengdu, Sichuan province, China (AUP 2015001B), and performed in compliance with the ARVO statement for the use of animals in ophthalmic and visual research.

Author contributions

DC designed the study, directed the project, and interpreted the data. RW, XR, HK, ZL, YC, YW, LX, TY, CL, and DC performed the experiments. SH and AN helped with FFA analysis. RB provided partial funds, reagents, and guidance for this project. DC and RB wrote the paper, and RW, XR, HK, ZL, YC, YT, YW, LX, TY, SH, CL, and AN contributed to editing.

Acknowledgments

We thank P Gruss, A Berns, G Leone, M Rudnicki, and M Greenberg for mice; CY Gregory-Evans and D Forrest for antibodies; K Zhao and W Sellers for plasmid vector; and Suying Lu for the luciferase reporter assay. This work was supported by grants to DC from the National Natural Science Foundation of China (81371022, 81570860, 81870665) and grants from the Canadian Institutes for Health Research, the Canadian Cancer Society Research Institute, the Krembil Foundation, and the Foundation Fighting Blindness Canada to RB.

Address correspondence to: Danian Chen, Room 224, Research Laboratory of Ophthalmology and Vision Sciences, State Key Laboratory of Biotherapy, West China Hospital, Sichuan University, 1 Keyuan 4th Road, Gaopeng Street, High Technological Development Zone, 610041, Chengdu, China. Phone: 18980605810; Email: danianchen2006@qq.com. Or to: Rod Bremner, Room 840, Lunenfeld-Tanenbaum Research Institute, Sinai Health System, 600 University Avenue, Toronto, Ontario, Canada M5G 1X5. Phone: 647.826.1525; Email: bremner@lunenfeld.ca.

1. Barben M, Samardzija M, Grimm C. The role of hypoxia, hypoxia-inducible factor (HIF), and VEGF in retinal angiomatous proliferation. *Adv Exp Med Biol*. 2018;1074:177–183.
2. Xin X, et al. Hypoxic retinal Muller cells promote vascular permeability by HIF-1-dependent upregulation of angiopoietin-like 4. *Proc Natl Acad Sci USA*. 2013;110(36):E3425–E3434.
3. Miller JW. Age-related macular degeneration revisited--piecing the puzzle: the LXIX Edward Jackson memorial lecture. *Am J Ophthalmol*. 2013;155(1):1–35.e13.
4. Yannuzzi LA, et al. Retinal angiomatous proliferation in age-related macular degeneration. *Retina (Philadelphia, Pa)*. 2001;21(5):416–434.
5. Monson DM, Smith JR, Klein ML, Wilson DJ. Clinicopathologic correlation of retinal angiomatous proliferation. *Arch Ophthalmol*. 2008;126(12):1664–1668.
6. Klein ML, Wilson DJ. Clinicopathologic correlation of choroidal and retinal neovascular lesions in age-related macular degeneration. *Am J Ophthalmol*. 2011;151(1):161–169.
7. Okamoto N, et al. Transgenic mice with increased expression of vascular endothelial growth factor in the retina: a new model of intraretinal and subretinal neovascularization. *Am J Pathol*. 1997;151(1):281–291.
8. Smith RS, John SW, Zabeleta A, Davisson MT, Hawes NL, Chang B. The bst locus on mouse chromosome 16 is associated with age-related subretinal neovascularization. *Proc Natl Acad Sci USA*. 2000;97(5):2191–2195.
9. Heckenlively JR, et al. Mouse model of subretinal neovascularization with choroidal anastomosis. *Retina (Philadelphia, Pa)*. 2003;23(4):518–522.
10. Weinl C, et al. Endothelial SRF/MRTF ablation causes vascular disease phenotypes in murine retinae. *J Clin Invest*. 2013;123(5):2193–2206.
11. Hasegawa E, et al. Characterization of a spontaneous retinal neovascular mouse model. *PLoS ONE*. 2014;9(9):e106507.
12. Park S, Chan CC. Von Hippel-Lindau disease (VHL): a need for a murine model with retinal hemangioblastoma. *Histol Histopathol*. 2012;27(8):975–984.
13. Lonser RR, et al. von Hippel-Lindau disease. *Lancet*. 2003;361(9374):2059–2067.
14. Semenza GL. Hypoxia-inducible factors in physiology and medicine. *Cell*. 2012;148(3):399–408.
15. Lobov IB, et al. WNT7b mediates macrophage-induced programmed cell death in patterning of the vasculature. *Nature*. 2005;437(7057):417–421.
16. Fruttiger M. Development of the retinal vasculature. *Angiogenesis*. 2007;10(2):77–88.
17. Jakobiec FA, Font RL, Johnson FB. Angiomatosis retinae. An ultrastructural study and lipid analysis. *Cancer*. 1976;38(5):2042–2056.

18. Grossniklaus HE, Thomas JW, Vigneswaran N, Jarrett WH. Retinal hemangioblastoma. A histologic, immunohistochemical, and ultrastructural evaluation. *Ophthalmology*. 1992;99(1):140–145.
19. Miyazawa A, Inoue M, Hirakata A, Okada AA, Iihara K, Fujioka Y. Expression of inhibin alpha by stromal cells of retinal angiomas excised from a patient with von Hippel-Lindau disease. *Jpn J Ophthalmol*. 2009;53(5):501–505.
20. Lange C, et al. Retina-specific activation of a sustained hypoxia-like response leads to severe retinal degeneration and loss of vision. *Neurobiol Dis*. 2011;41(1):119–130.
21. Kurihara T, et al. von Hippel-Lindau protein regulates transition from the fetal to the adult circulatory system in retina. *Development*. 2010;137(9):1563–1571.
22. Arreola A, et al. Von Hippel-Lindau mutations disrupt vascular patterning and maturation via Notch. *JCI Insight*. 2018;3(4):92193.
23. Usui Y, et al. Neurovascular crosstalk between interneurons and capillaries is required for vision. J Clin Invest. 2015;125(6):2335–2346.
24. Lange C, et al. Normoxic activation of hypoxia-inducible factors in photoreceptors provides transient protection against light-induced retinal degeneration. *Invest Ophthalmol Vis Sci*. 2011;52(8):5872–5880.
25. Barben M, Schori C, Samardzija M, Grimm C. Targeting Hif1a rescues cone degeneration and prevents subretinal neovascularization in a model of chronic hypoxia. *Mol Neurodegener*. 2018;13(1):12.
26. Lange CA, et al. Von Hippel-Lindau protein in the RPE is essential for normal ocular growth and vascular development. *Development*. 2012;139(13):2340–2350.
27. Wang H, et al. Deletion of the von Hippel-Lindau gene in hemangioblasts causes hemangioblastoma-like lesions in murine retina. Cancer Res. 2018;78(5):1266–1274.
28. Mehrian-Shai R, et al. Identification of genomic aberrations in hemangioblastoma by droplet digital PCR and SNP microarray highlights novel candidate genes and pathways for pathogenesis. BMC Genomics. 2016;17.
29. Harlander S, et al. Combined mutation in Vhl, Trp53 and Rb1 causes clear cell renal cell carcinoma in mice. *Nat Med*. 2017;23(7):869–877.
30. Zhang H, et al. Mitochondrial autophagy is an HIF-1-dependent adaptive metabolic response to hypoxia. *J Biol Chem*. 2008;283(16):10892–10903.
31. Bellot G, et al. Hypoxia-induced autophagy is mediated through hypoxia-inducible factor induction of BNIP3 and BNIP3L via their BH3 domains. Mol Cell Biol. 2009;29(10):2570–2581.
32. Wang Y, Abu-Asab MS, Shen D, Zhuang Z, Chew EY, Chan CC. Upregulation of hypoxia-inducible factors and autophagy in von Hippel-Lindau-associated retinal hemangioblastoma. *Graefes Arch Clin Exp Ophthalmol*. 2014;252(8):1319–1327.
33. Burkhart DL, Sage J. Cellular mechanisms of tumor suppression by the retinoblastoma gene. *Nat Rev Cancer*. 2008;8(9):671–682.
34. Chen D, Livne-bar I, Vanderluit JL, Slack RS, Agochiya M, Bremner R. Cell-specific effects of RB or RB/p107 loss on retinal development implicate an intrinsically death-resistant cell-of-origin in retinoblastoma. *Cancer Cell*. 2004;5(6):539–551.
35. MacPherson D, Sage J, Kim T, Ho D, McLaughlin ME, Jacks T. Cell type-specific effects of Rb deletion in the murine retina. *Genes Dev*. 2004;18(14):1681–1694.
36. Zhang J, Schweers B, Dyer MA. The first knockout mouse model of retinoblastoma. *Cell Cycle*. 2004;3(7):952–959.
37. Tracy K, Dibling BC, Spike BT, Knabb JR, Schumacker P, Macleod KF. BNIP3 is an RB/E2F target gene required for hypoxia-induced autophagy. *Mol Cell Biol*. 2007;27(17):6229–6242.
38. Bakker WJ, Weijts BG, Westendorp B, de Bruin A. HIF proteins connect the RB-E2F factors to angiogenesis. *Transcription*. 2013;4(2):62–66.
39. Budde A, Schneiderhan-Marra N, Petersen G, Brüne B. Retinoblastoma susceptibility gene product pRB activates hypoxia-inducible factor-1 (HIF-1). *Oncogene*. 2005;24(10):1802–1808.
40. Zhou Y, et al. Rb is required for retinal angiogenesis and lamination. *Cell Death Dis*. 2018;9(3):370.
41. Sicinski P, et al. Cyclin D1 provides a link between development and oncogenesis in the retina and breast. *Cell*. 1995;82(4):621–630.
42. Marquardt T, Ashery-Padan R, Andrejewski N, Scardigli R, Guillemot F, Gruss P. Pax6 is required for the multipotent state of retinal progenitor cells. *Cell*. 2001;105(1):43–55.
43. Li S, et al. Retro-orbital injection of FITC-dextran is an effective and economical method for observing mouse retinal vessels. *Mol Vis*. 2011;17:3566–3573.
44. Chen D, et al. Rb-mediated neuronal differentiation through cell-cycle-independent regulation of E2f3a. *PLoS Biol*. 2007;5(7):e179.
45. Zhao WT, et al. The von Hippel-Lindau protein pVHL inhibits ribosome biogenesis and protein synthesis. *J Biol Chem*. 2013;288(23):16588–16597.
46. Piret JP, Mottet D, Raes M, Michiels C. CoCl2, a chemical inducer of hypoxia-inducible factor-1, and hypoxia reduce apoptotic cell death in hepatoma cell line HepG2. *Ann N Y Acad Sci*. 2002;973:443–447.
47. Qin G, et al. Cell cycle regulator E2F1 modulates angiogenesis via p53-dependent transcriptional control of VEGF. *Proc Natl Acad Sci USA*. 2006;103(29):11015–11020.
48. Caprara C, Thiersch M, Lange C, Joly S, Samardzija M, Grimm C. HIF1A is essential for the development of the intermediate plexus of the retinal vasculature. *Invest Ophthalmol Vis Sci*. 2011;52(5):2109–2117.
49. Otani A, et al. Rescue of retinal degeneration by intravitreally injected adult bone marrow-derived lineage-negative hematopoietic stem cells. *J Clin Invest*. 2004;114(6):765–774.
50. Chen D, Pacal M, Wenzel P, Knoepfler PS, Leone G, Bremner R. Division and apoptosis of E2f-deficient retinal progenitors. *Nature*. 2009;462(7275):925–929.
51. Bienvenu F, et al. Transcriptional role of cyclin D1 in development revealed by a genetic-proteomic screen. *Nature*. 2010;463(7279):374–378.
52. Gossage L, Eisen T, Maher ER. VHL, the story of a tumor suppressor gene. *Nat Rev Cancer*. 2015;15(1):55–64.
53. Young AP, et al. VHL loss actuates a HIF-independent senescence programme mediated by Rb and p400. *Nat Cell Biol*. 2008;10(3):361–369.
54. Haase VH, Glickman JN, Socolovsky M, Jaenisch R. Vascular tumors in livers with targeted inactivation of the von Hippel-Lindau

tumor suppressor. *Proc Natl Acad Sci USA*. 2001;98(4):1583–1588.
55. Al-Salam S, Al-Salam M, Al Ashari M. Galectin-3: a novel protein in cerebellar hemangioblastoma. *Int J Clin Exp Pathol*. 2013;6(5):853–861.
56. Bauer PM, Zalis MC, Abdshill H, Deierborg T, Johansson F, Englund-Johansson U. Inflamed in vitro retina: cytotoxic neuroinflammation and galectin-3 expression. *PLoS One*. 2016;11(9):e0161723.
57. Masuda T, et al. Transcription factor SOX9 plays a key role in the regulation of visual cycle gene expression in the retinal pigment epithelium. *J Biol Chem*. 2014;289(18):12908–12921.
58. Vintersten K, et al. Mouse in red: red fluorescent protein expression in mouse ES cells, embryos, and adult animals. *Genesis*. 2004;40(4):241–246.
59. Berger AH, Knudson AG, Pandolfi PP. A continuum model for tumor suppression. *Nature*. 2011;476(7359):163–169.
60. Gonzalez-Vasconcellos I, Anastasov N, Sanli-Bonazzi B, Klymenko O, Atkinson MJ, Rosemann M. Rb1 haploinsufficiency promotes telomere attrition and radiation-induced genomic instability. *Cancer Res*. 2013;73(14):4247–4255.
61. Coschi CH, et al. Haploinsufficiency of an RB-E2F1-Condensin II complex leads to aberrant replication and aneuploidy. *Cancer Discov*. 2014;4(7):840–853.
62. Lum JJ, et al. Growth factor regulation of autophagy and cell survival in the absence of apoptosis. *Cell*. 2005;120(2):237–248.
63. Dasgupta P, et al. Nicotine induces cell proliferation by beta-arrestin-mediated activation of Src and Rb-Raf-1 pathways. *J Clin Invest*. 2006;116(8):2208–2217.
64. Filomeni G, De Zio D, Cecconi F. Oxidative stress and autophagy: the clash between damage and metabolic needs. *Cell Death Differ*. 2015;22(3):377–388.
65. Keith B, Johnson RS, Simon MC. HIF1α and HIF2α: sibling rivalry in hypoxic tumor growth and progression. *Nat Rev Cancer*. 2011;12(1):9–22.
66. Bibb LC, et al. Temporal and spatial expression patterns of the CRX transcription factor and its downstream targets. Critical differences during human and mouse eye development. *Hum Mol Genet*. 2001;10(15):1571–1579.
67. Ng L, Ma M, Curran T, Forrest D. Developmental expression of thyroid hormone receptor beta2 protein in cone photoreceptors in the mouse. *Neuroreport*. 2009;20(6):627–631.
68. Liu Y, et al. Next-generation RNA sequencing of archival formalin-fixed paraffin-embedded urothelial bladder cancer. *Eur Urol*. 2014;66(6):982–986.
69. Gregorieff A, Liu Y, Inanlou MR, Khomchuk Y, Wrana JL. Yap-dependent reprogramming of Lgr5(+) stem cells drives intestinal regeneration and cancer. *Nature*. 2015;526(7575):715–718.
70. Babicki S, et al. Heatmapper: web-enabled heat mapping for all. *Nucleic Acids Res*. 2016;44(W1):W147–W153.
71. Chen EY, et al. Enrichr: interactive and collaborative HTML5 gene list enrichment analysis tool. *BMC Bioinformatics*. 2013;14:128.
72. Kuleshov MV, et al. Enrichr: a comprehensive gene set enrichment analysis web server 2016 update. *Nucleic Acids Res*. 2016;44(W1):W90–W97.
73. Wang Y, Zhou Y, Xiao L, Zheng S, Yan N, Chen D. E2f1 mediates high glucose-induced neuronal death in cultured mouse retinal explants. *Cell Cycle*. 2017;16(19):1824–1834.
74. Zheng S, et al. DZNep inhibits H3K27me3 deposition and delays retinal degeneration in the rd1 mice. *Cell Death Dis*. 2018;9(3):310.
75. Liu R, Liu H, Chen X, Kirby M, Brown PO, Zhao K. Regulation of CSF1 promoter by the SWI/SNF-like BAF complex. *Cell*. 2001;106(3):309–318.
76. Sellers WR, et al. Stable binding to E2F is not required for the retinoblastoma protein to activate transcription, promote differentiation, and suppress tumor cell growth. *Genes Dev*. 1998;12(1):95–106.
77. Ni Z, et al. Apical role for BRG1 in cytokine-induced promoter assembly. *Proc Natl Acad Sci USA*. 2005;102(41):14611–14616.